metals

Article

Evaluation of Crashworthiness Using High-Speed Imaging, 3D Digital Image Correlation, and Finite Element Analysis

Simon Jonsson * and Jörgen Kajberg

Division of Solid Mechanics, Luleå University of Technology, 971 87 Luleå, Sweden; jorgen.kajberg@ltu.se
* Correspondence: simon.jonsson@ltu.se

Abstract: To promote the use of new high-strength materials in the automotive industry, the evaluation of crashworthiness is essential, both in terms of finite element (FE) analysis as well as validation experiments. This work proposes an approach to address the crash performance through high-speed imaging combined with 3D digital image correlation (3D-DIC). By tracking the deformation of the component continuously, cracks can be identified and coupled to the load and intrusion history of the experiment. The so-called crash index (CI) and its decreasing rate (CIDR) can then be estimated using only one single (or a few) component, instead of a set of components with different levels of intrusion and crushing. Crash boxes were axially and dynamically compressed to evaluate the crashworthiness of TRIP-aided bainite ferrite steel and press-hardenable steel. A calibrated rate-dependent constitutive model, and a phenomenological damage model were used to simulate the crash box testing. The absorbed energy, the plastic deformation, and the CIDR were evaluated and compared to the experimentally counterparts. When applying the proposed method to evaluate the CIDR, a good agreement was found when using CI:s reported by other authors using large sets of crash boxes. The FE analyses showed a fairly good agreement with some underestimation in terms of energy absorptions. The crack formation was overestimated resulting in too high a predicted CIDR. It is concluded that the proposed method to evaluate the crashworthiness is promising. To improve the modelling accuracy, better prediction of the crack formation is needed and the introduction of the intrinsic material property, fracture toughness, is suggested for future investigations and model improvements.

Keywords: crashworthiness; crash index; third-generation AHSS; 3D digital image correlation; high strain rate; damage modelling

Citation: Jonsson, S.; Kajberg, J. Evaluation of Crashworthiness Using High-Speed Imaging, 3D Digital Image Correlation, and Finite Element Analysis. *Metals* **2023**, *13*, 1834. https://doi.org/10.3390/met13111834

Academic Editors: Denis Benasciutti, Luis Reis and Julian M. E. Marques

Received: 29 September 2023
Revised: 19 October 2023
Accepted: 26 October 2023
Published: 31 October 2023

1. Introduction

The automotive industry is currently undergoing drastic changes to embrace the progressively stringent emission regulations in the automotive sector. The current electrification of the automotive fleet to remove tailpipe emissions altogether, although accelerating, is still in its infancy with a large majority of the cars currently sold having a conventional internal combustion engine (ICE). It is well documented that the vehicle operation phase is the largest contributor to the life-cycle energy and greenhouse gas (GHG) emissions for conventional ICE light-duty vehicles [1–5] mainly because of the tailpipe emissions from burning fuel. Due to the fuel consumption's dependency on mass [6–8], reducing the weight of the vehicles can significantly reduce their carbon footprint. This can be done by using lightweight materials such as aluminium alloys, carbon-fibre materials, or even additive manufacturing (AM) to reduce the curb weight of the vehicle [9]. However, weight reduction in the use phase does not guarantee an improved environmental impact when the whole life cycle of the vehicle is considered [10], often because of increased energy consumption in manufacturing and difficulties with recycling after the end of its life. Since steel has the advantage of being cheap and easily recycled after the end of its life [11,12], an alternative to material substitution is thus to downgauge the thickness of the steel sheets used when stamping components, but achieving this without compromising structural stiffness and crash performance require higher-strength steel grades. Increasing the strength of the steel might however negatively impact the formability of the components due to springback, and high-strength steel can be more prone to cracking when forming [13,14]. In recent years, third-generation advanced high-strength steels (AHSSs) offering an excellent combination of high strength and ductility have started to gain traction in the automotive industry. This generation aims to close the gap between the previous first-generation AHSS and the expensive, complex, twinning-induced second-generation AHSS. New generations of press-hardening steels (PHS) are also being developed offering an excellent combination of high strength and good local ductility allowing for more complex component shapes to be formed without the springback sometimes present in the cold forming of high-strength steels [15].

To encourage the application of these new high-strength steel grades on an industrial scale, it is important to accurately simulate manufacturing processes such as forming and to predict the final product performance. The FE analysis has, over the years, become a helpful tool in industry design. The accuracy of the modelled processes and design steps relies on precise material models describing the mechanical properties in terms of, e.g., flow stress behaviour, ductility, and fracture characteristics. This has led to a large experimental effort to investigate these new steel grades in recent years, and a large comprehensive study on commercially available third-generation AHSS was recently performed where constitutive, formability, tribology, and fracture behaviour were all evaluated and compared to the previous-generation AHSS [16]. The study showed that the enhanced global formability did not necessarily transfer to local formability. Similar conclusions regarding local ductility were made by other authors, who evaluated fracture resistance of different first- and third-generation AHSS grades with tensile strengths ranging from 780 to 1180 MPa [17]. A recent study of the flow behaviour to fracture of four 1180 MPa third-generation AHSS grades showed that the strength increased with strain rate for all investigated materials even though the total elongation differed [18]. Furthermore, the fracture toughness of AHSS grades has also been shown to increase with strain-rate [19]. Hence, it is necessary to test these grades using different loading rates and different stress states in order to accurately capture their constitutive and fracture behaviours.

Due to the attractive combination of strength and ductility, the recent generations of AHSS have become popular in body-in-white, and especially energy-absorbing safety parts. Since full-scale component testing is cumbersome and expensive, the FE analysis has become a helpful tool in industry design and crashworthiness evaluation. Because of the large plastic strains involved, data regarding the flow stress and strains beyond diffuse necking all the way to fracture are needed. Typically, material models for these conditions are calibrated using extensive inverse modelling, which may be a complicated and time-consuming process. Recently, a direct method, the stepwise modelling method (SMM), to obtain the flow stress past initial yielding to final fracture using 2D digital image correlation has been published [20–22]. The method was initially developed for isotropic materials but was later established for anisotropic materials as well [23]. The method works for different stress states and gives the evolution of the triaxiality as a function of the equivalent plastic strain. SMM has been successfully used to characterise the hardening behaviour [21] and to calibrate different fracture loci [24].

However, to prove the predictability of the simulation models, it is of crucial importance to validate them to full-scale experimental component testing. In the automotive industry, axial compression and three-point bending tests of crash boxes are often the components of choice since these are used for energy absorption and anti-intrusion in vehicles to protect the passengers. These are usually performed using an accelerated mass where the deformation intensity is generally controlled by modifying the load mass speed. The crashworthiness of the components is determined from the severity of cracking, sometimes quantified with a crash index (CI). Such indices based on visual inspection have been published by other authors, both for axial compression [25,26] and three-point bending [27].

In order to take damage evolution into account and to circumvent the difficulties with spot welds, Frómeta et al. [28] proposed a crash index decreasing rate (CIDR). However, to obtain the CIDR, several axial compression tests are generally needed at different crushing depths to determine the crash index evolution, costing both time and material.

This work proposes an alternative approach to address crash performance through high-speed imaging together with 3D digital image correlation (3D-DIC). By tracking the deformation of the component continuously from start to finish, the initiation of cracks and their propagation can be identified and coupled to the load and intrusion history of the experiment. In addition to enabling crashworthiness to be evaluated in terms of CIDR with less crash box tests, the damage evolution can be further investigated to validate crashworthiness simulations. Two AHSS grades are selected, a 1180 MPa third-generation TRIP AHSS grade for cold-stamping applications and a 1000 MPa PHS steel grade for hot-stamping applications, and the constitutive and fracture behaviour are investigated at different strain rates and stress states. An isotropic version of a previously published SMM [20,21] is utilised to calibrate a viscoplastic hardening model and an empirically based fracture locus implemented in the commercial FE code LS-DYNA®. In order to validate the crashworthiness simulations, the results from the FE analyses are then compared to the experimental results from the crash box tests using high-speed imaging and 3D-DIC.

This paper therefore presents the whole cycle of characterising materials using an SMM, implementing the material and damage model into a finite element model of the crash box, and finally performing a detailed validation of the simulation results. To summarise, this paper aims to contribute with the following:

- An evaluation of the strain-rate sensitivity on the hardening response and the fracture behaviour at various stress triaxialities for a 1180 MPa third-generation AHSS and a 1000 MPa PHS.
- The development of a high-speed axial compression test using a pair of high-speed cameras and 3D-DIC to follow the crushing response, crack formation, and subsequent propagation. An evaluation of crashworthiness through the use of CIDR.
- The validation of calibrated material and damage models by comparing a commercial FE analysis with experimental results from axial compression tests.

2. Materials and Model Calibration

2.1. Materials

In this article, a 3rd-generation trip-aided bainite ferrite (TBF) steel with a specified ultimate tensile strength (UTS) of 1180 MPa for cold-stamping applications, as well as a press-hardened steel with a specified UTS of 1000 MPa were investigated. Both industrial steel grades were provided by ArcelorMittal. The 3rd-generation TBF steel has a fine carbide-free bainitic matrix with islands of martensite/retained austenite as well as laths of retained austenite [17]. The chemical composition in weight percent for the TBF steel grade is presented in Table 1. The PHS steel grade is a boron steel with a mainly martensitic microstructure after heat treatment. The chemical composition in weight percent for the PHS steel grade is presented in Table 2.

Table 1. Chemical composition in weight percent for the 3rd-generation TBF steel used in the experiments. The balance is Fe. (* Max).

C	Si	Mn	P	S	Al	Cu	B	Ti + Nb	Cr + Mo
0.26 *	2.2 *	3.0 *	0.05 *	0.01 *	0.015–2.0*	0.20 *	0.005 *	0.15 *	1.4 *

Table 2. Chemical composition in weight percent for the press-hardening steel (PHS) grade used in the experiments. The balance is Fe. (* Max).

C	Si	Mn	P	S	Al	Ti	Nb	Cu	B	Cr
0.10 *	0.6 *	1.8 *	0.03 *	0.01 *	0.01–0.1	0.05 *	0.10 *	0.20 *	0.005 *	0.20 *

2.2. Mechanical Material Characterisation

In crash scenarios, typically, large strains and high strain rates are present. It is therefore crucial that the selected material models take those conditions into consideration, and a set of appropriate tests must therefore be applied. Testing at various strain rates from 1 s^{-1} to 100 s^{-1} were therefore conducted for various stress states to investigate the rate dependence on the flow stress and fracture strains. In crash scenarios, the strain rates can reach well above 1000 s^{-1}, but these strain rates were not achievable with the tensile testing machine used in this study for the selected geometries. The SMM was used to get the post-yield flow stress behaviour. Due to the relatively low anisotropy reported in previous investigations of AHSS grades [16,29–32], this article took advantage of the isotropic version of the SMM with a von Mises yield criterion to characterise the material flow behaviour and to calibrate a plane-stress failure locus.

2.2.1. Tensile Testing

In order to document the strain rate dependence of the grades, regular tensile tests on straight specimens were conducted for the two grades. Tests were conducted for quasi-static conditions as well as at strain rates of 1, 10, and 100 s^{-1}. The uniform elongation was measured with a Zimmer 100D (Zimmer OHG, D-6101, Rossdorf/Darmstadt, West Germany) non-contacting displacement transducer with a gauge length of 50 mm. The geometries used for the quasi-static testing and the high-speed tests are presented in Figure 1. The quasi-static tests were performed in a servo-hydraulic Instron (Norwood, MA, USA) 1272 tensile testing machine with a grip speed of 4 mm/minute and the high-speed tests were performed in a hydraulic Instron VHS160/100-20 tensile testing machine with a grip speed of 65 mm/s, 650 mm/s, and 6500 mm/s, respectively.

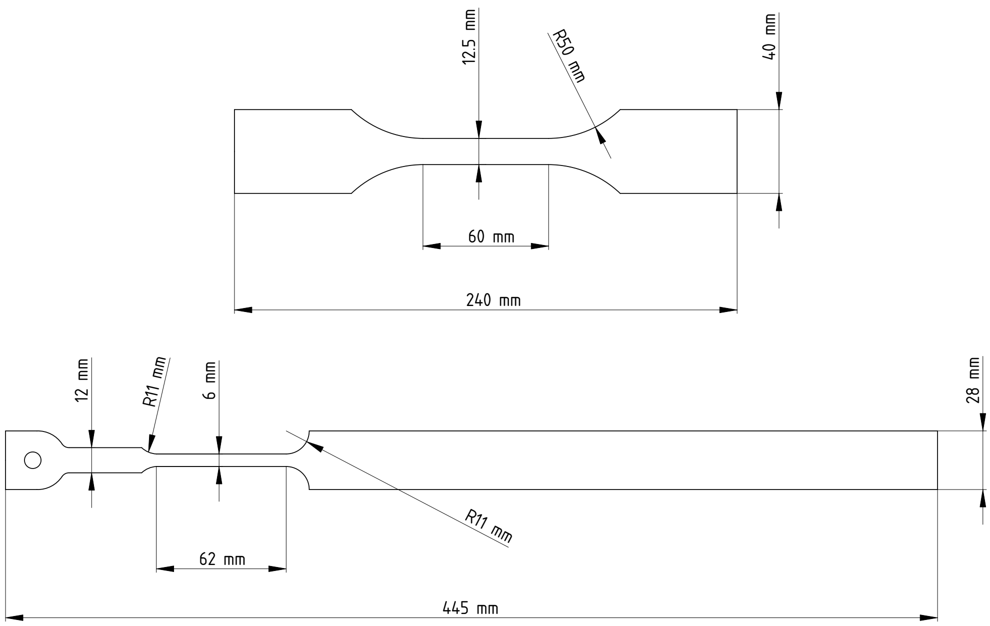

Figure 1. The straight tensile geometries used to test the strain rate dependency of the two grades. The upper geometry was used for the quasi-static experiments and the lower was used for high-speed testing.

To investigate the material behaviour for different stress states and to calibrate a plane-stress fracture criterion, a set of dynamic tensile tests with different geometries to capture the different stress states was performed. High-speed imaging using a Vision Research Phantom high-speed camera was combined with 2D-DIC to determine the strain fields on the specimen surfaces. Four geometries were used: a shear specimen ($\eta = 0$), a hole specimen to capture the uniaxial stress state ($\eta = 1/3$), a notched specimen with a radius of 15 mm ($\eta \approx 0.45$), and a notched specimen with a radius of 3.75 mm ($\eta \approx 0.58$) to represent the plane strain state. These triaxiality values should be seen as average values since the notched specimens especially tend to drift towards plane strain territory close to fracture. The gauge area of these geometries can be seen (in order from left to right) in Figure 2 with full geometries presented in previously published papers [24,33]. These tests were only performed for high strain rates and not quasi-static conditions since higher strain rates dominate in typical crash situations. The gauge areas were covered with a randomised speckle pattern for the 2D-DIC evaluation with the settings for the different geometries presented in Tables A1 and A2 for the TBF 1180 and PHS 1000 grade, respectively. The qualitative strain field distribution of the different geometries is presented in Figure 3. This technique is well established and described in detail by others [34].

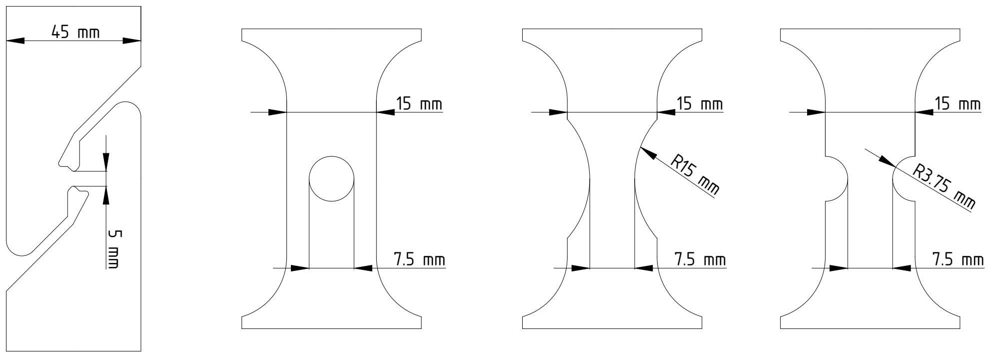

Figure 2. The gauge area of the different sheet tensile specimen used to capture different triaxialities. From left to right: shear specimen, hole specimen, notched specimen with a 15 mm radius, and notched specimen with a 3.75 mm radius.

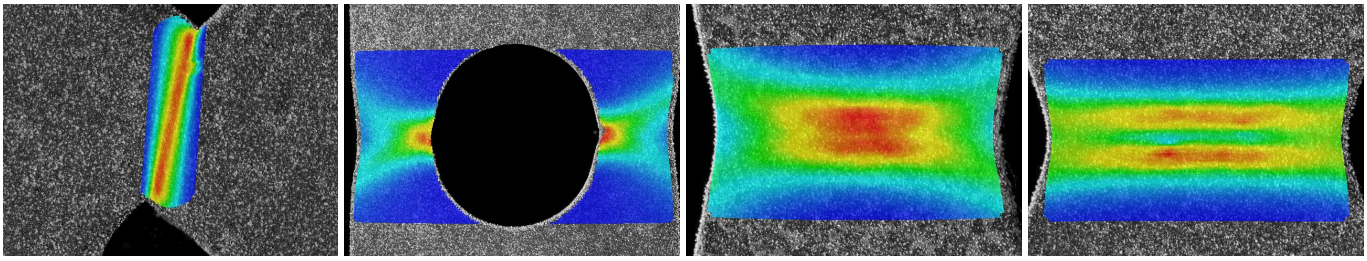

Figure 3. Qualitative strain field distribution in 2D DIC images of the shear, hole, and the two notched tensile specimens presented in Figure 2 from left to right.

2.2.2. Model Calibration

Since the selected grades were tested at different strain rates, a rate-dependent flow stress model was considered. Here, a simplified Johnson–Cook flow stress model [35] was used, given by

$$\sigma = (A + B\varepsilon^n)\left(1 + C \cdot \ln\frac{\dot{\varepsilon}}{\dot{\varepsilon}_0}\right) \tag{1}$$

where ε is the equivalent plastic strain and $\dot{\varepsilon}/\dot{\varepsilon}_0$ is the dimensionless plastic strain rate, where $\dot{\varepsilon}_0$ was set to 1 s^{-1}. The material parameter A is related to the yield stress, while B and n controls the strain-hardening effect. The parameter C is coupled to the strain rate dependency of the material. These parameters were obtained using curve fitting on flow curves from the SMM.

When it comes to characterising fracture, it is well documented that the stress state, or stress triaxiality η, defined as the ratio of the mean stress σ_m and effective stress σ_{eff}, has a large influence on the ductile fracture of a material [36–41]. Additionally, the third deviatoric invariant of the stress tensor, the Lode angle, also has an influence. For accurate modelling, especially in complex crash scenarios, this must be considered in the fracture criterion, and several empirical fracture models exist, see, e.g., [42–44]. In contrast to physically based models, these are calibrated using an extensive testing of the bulk material in different settings to verify how it behaves in various loading conditions. The results are then later combined into a fracture locus in the form of a curve (for shells) or surface (for solids). This is attractive from an engineering point-of-view since calibration experiments are relatively simple and can be conducted with ease in a lab. In this study, the phenomenological modified Mohr–Coulomb (MMC) model with a von Mises yield function proposed by Bai and Wierzbicki [45] was used as the fracture locus and is presented in Equation (2).

$$\bar{\varepsilon}_f = \left\{ \frac{A}{c_2} \left[\sqrt{\frac{1+c_1^2}{3}} \cos\left(\frac{\bar{\theta}\pi}{6}\right) + c_1 \left(\eta + \frac{1}{3} \sin\left(\frac{\bar{\theta}\pi}{6}\right) \right) \right] \right\}^{-\frac{1}{n}} \tag{2}$$

The equivalent fracture strain is a function of the stress triaxiality η and the normalised lode angle parameters $\bar{\theta}$. The parameter A is coupled to the yield stress of the material and was thus set to the same yield parameter as in the Johnson–Cook Equation (1) model in this study. Both A and c_2 are essentially scaling parameters for the fracture locus, while c_1 is describing the pressure dependency of the fracture strain with $c_1 = 0$ indicating a perfectly symmetric fracture locus with respect to the Lode parameter [45]. If plane stress is assumed, there is a relation between this parameter and the stress triaxiality given by Equation (3).

$$\bar{\theta} = 1 - \frac{2}{\pi} \arccos\left(-\frac{27}{2}\eta\left(\eta^2 - \frac{1}{3}\right)\right) \tag{3}$$

The MMC failure criterion was calibrated with a set of tensile tests of different geometries, presented in Figure 2, to capture different stress states in monotonic loading. However, since monotonic loading is hard to achieve and the stress triaxiality varies during loading, an integrated average triaxiality was used according to Equation (4). A similar approach was used in [22,43,46]. This is a simplification, since it is questionable that the fracture strain as a function of the average triaxiality is accessible experimentally for the entire triaxiality range [47,48]. However, other authors using similar fracture calibration have shown promising results [49] for other load cases.

$$\eta_{int} = \frac{1}{\bar{\varepsilon}_f^p} \int_0^{\bar{\varepsilon}_f^p} \eta(\bar{\varepsilon}^p) d\bar{\varepsilon}^p \tag{4}$$

3. Crashworthiness—Test and Evaluation

Crashworthiness is defined as the ability of a structure to protect its occupants in a crash. Briefly, a modern vehicle today consists of a passenger safety cage with two deformation zones. The role of the safety cage is to protect the occupants by limiting intrusion into the compartment, demanding high-strength materials with high ultimate load before failure. The role of the front and rear deformation zones are instead to absorb the impact energy and crumple in a predictable manner, making a more ductile material suitable. The energy absorption capability of a material in these crumple zones is thus crucial for the crashworthiness of the vehicle. To evaluate the performance of a material for these applications, dynamic axial compression tests of crash boxes are usually performed. Thus, to evaluate the crashworthiness of the two selected AHSSs, and to validate the calibrated materials models, dynamic axial compression tests were performed.

3.1. Axial Compression Experiments

Different crash box geometries with the same bulk length of 300 mm were used for the two tested grades with the cross-section dimensions labelled in Figure 4. To the left is the geometry used for the TBF 1180 steel grade which was cold-formed, and to the right is the geometry used for the PHS 1000 steel grade which was hot-formed. In order to stabilise the crash boxes, a spot-welded closing bank was added to the bottom. The welds were located approximately 15 mm from both edges on the flange and then successively placed with approximately 30 mm gaps. The crash box's axial compression setup is presented in Figure 5. The crash boxes were compressed in a high-speed machine, Instron VHS160/100-20, at approximately 20 m/s. To enable full-field deformation measurements using 3D-DIC, two high-speed cameras, Vision Research Phantom v1610 and v2512, were placed in front of the crash boxes separated with an angle of 23 degrees. This test setup with a servo-hydraulic machine instead of a drop tower allowed for flexibility in the tuning of compression speed. Because of the limited load cell capacity, the crash boxes had to be precrushed approximately 15–20 mm by the manufacturer at quasi-static speed (10 mm/min) in order to avoid the initial load peak. A frame rate of 24,000 frames per second was used resulting in a spatial resolution of 800 $\times$ 640 pixels. That frame rate combined with the spatial resolution was considered as a good compromise between the temporal and spatial resolution. The crash boxes were prepared by first sandblasting the top surface and then applying a randomised speckle pattern (using black and white spray paint) in order to track the plastic deformation, crack initiations, and the following propagation using 3D-DIC with the settings presented in Table A3. To avoid aliasing, the speckle size should be at least 3 pixels [50,51]. The speckle sizes in all conducted experiments were approx. 3 to 4 pixels. The details on how to obtain the sizes are presented in Appendix A. In addition to the deformation fields, the force and displacement histories were also tracked in order to evaluate the crashworthiness of the components and to give input to the FE analyses.

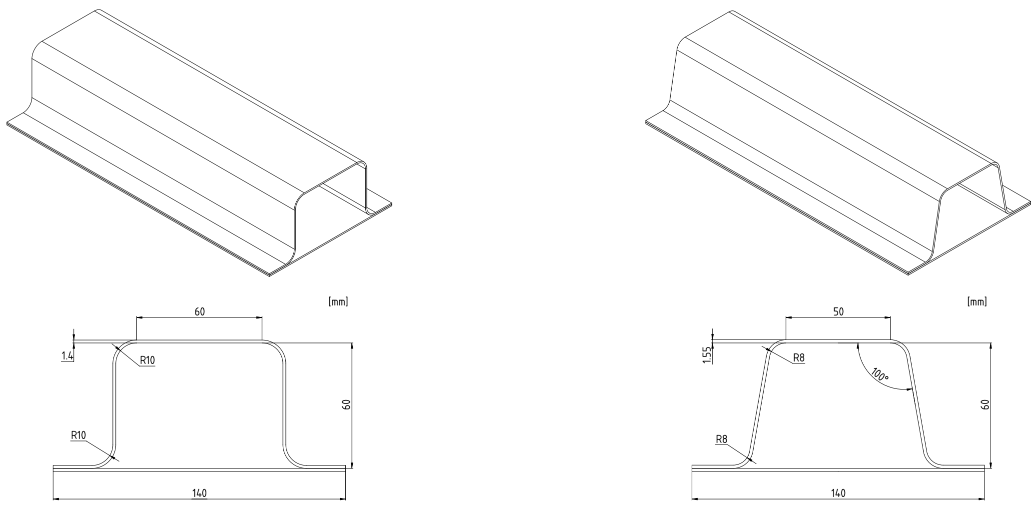

Figure 4. The two crash box geometries used in the axial compression test. To the left is the geometry used for the TBF 1180 steel grade and to the right is the geometry used for the PHS 1000 steel grade. The bulk length of both crash boxes was 300 mm before pre-crush.

Figure 5. The stereo high-speed camera setup in the high-speed hydraulic tensile machine for the crash box experiments.

3.2. Crashworthiness Evaluation

Energy absorption and deformation predictability of crash boxes under axial compression are crucial for the safety of the vehicle. Since cracks have a detrimental effect on these properties, the impact performance can be quantified using a crash index (CI) based on the extent of cracking of the material after impact [25–27]. The method involves deforming a component and then measuring the extent of cracking in the bulk material postexperiment using visual inspection. The more extensive the cracking after deformation, the lower the CI factor becomes and thus the lower the impact performance. Different CI factors exist, some based on the average crack length in the component [26] and some using the total crack length with different weightings for surface and through-thickness cracks [27]. Since cracks can be hard to measure in dynamic axial compression due to folding, the maximum through thickness crack length detected in the crash box component was used in this work together with the CI definition proposed by Larour et al. [25]. This definition is presented in Figure 6 (left) with the CI rating given in percent and separated into a set of groups ranging from poor CI (below 25%) with multiple breaks and splitting to a CI of 100% for components with no cracking after crush. Materials with a very low CI are not suitable for energy absorption application such as crash boxes under axial compression but can have other applications such as anti-intrusion components under impact bending.

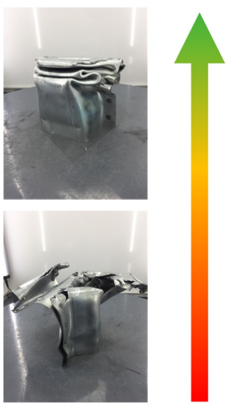

Crash index [%]	Crack length [mm]
100 (++)	No cracking
>75 (+)	<10
50-75 (+/−)	10–25
25-50 (−)	>25
<25 (−−)	Multiple breaks, splitting

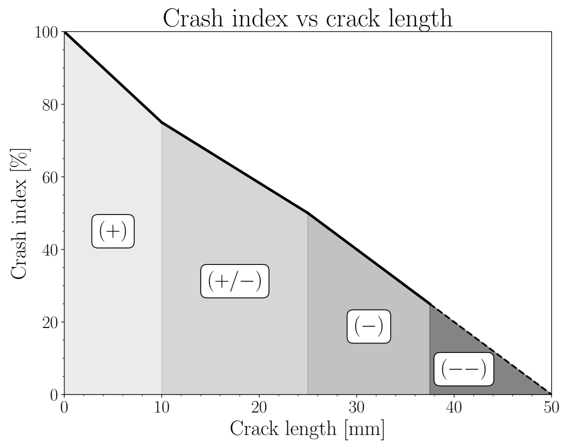

Figure 6. (**Left**): Crash index definition adapted from Larour et al. [25] used to rate the material deterioration in axial compression. A low crash index indicates more cracks and a lower impact performance. Materials with a low CI are generally not suitable for energy absorption applications. (**Right**): Proposed linear interpolation between the limit values. A CI below 25% is proposed to deteriorate linearly with the same slope as the previous segment.

Although the limit values (CI of 100, 75, 50, 25, or 0 percent) might generally be sufficient for a postexperiment evaluation of crash boxes, the definition is somewhat vague between the limiting values. When comparing to FE analyses, where detailed information is easily accessible, or when more accurate measurements are available, it is however also interesting to track intermediate values of the crack lengths. For this reason, a linear interpolation between the limiting levels is proposed according to Figure 6 (right). A CI below 25% is proposed to deteriorate linearly with the same slope as the previous (–) segment. Thus, a crushed component with any cracks larger than 50 mm is given a CI of zero.

One limitation of using the CI is that it does not give any information about the location or cause of the crack initiation. Fractured spot welds can drastically change the loading condition of the component, which can promote the extensive formation of cracks which would have otherwise not been formed. This can lead to spurious results that do not properly describe the part performance, because only cracks in the bulk material should be considered to assess the material performance [26]. Furthermore, the CI rating is naturally coupled to the intrusion level of a specific crash box experiment, and thus no information about the damage evolution is available. To circumvent this, a crash index decreasing rate (CIDR) [28] can be used to evaluate the crashworthiness. It quantifies the crash resistance of the material by tracking the evolution of cracks using a linear regression beyond the critical intrusion (material starting to crack) to the lowest measured crash index (at maximum intrusion) in a series of impact tests, regardless of the crack initiation cause, which simplifies the evaluation significantly. However, to obtain the CIDR, several axial compression tests are generally needed at different crushing depths to determine the crash index evolution, costing both time and material.

Due to the linear nature of the CIDR, it opens up the possibility to reduce the number of crash box tests by using high-speed imaging to track the intrusion process. By studying the CIDR results from the extensive crash box testing conducted by Frómeta et al. [28], two critical measuring points could be determined, namely the critical intrusion (the intrusion level where the material starts to crack, i.e., when the CI dips below 100) and the CI at maximum intrusion. Reproduced results (The points were estimated from scatter plots since no raw data were available, and thus the exact CIDR values could not be reproduced. The overall trends are however similar enough.) from three of the nine tested steel grades are presented in Figure 7 (left) together with a plot where a linear interpolation between the critical intrusion and CI at maximum intrusion for each grade, respectively (right). It is readily shown that interpolating between these critical points gives a good estimation of the evaluated CIDR based on a larger set of boxes. One should keep in mind that there are uncertainties already introduced in the method because of subjectivity concerning detecting cracks and deciding their lengths. By choosing a critical intrusion of 75%, corresponding to cracks with lengths of 10 mm, which are relatively easy to detect using high-speed imaging combined with 3D-DIC, this critical point could be estimated with satisfactory accuracy. By setting the critical intrusion to 75% for each of the steel grades in Figure 7, the results changed from 0.45 to 0.33 for the CP steel grade and from 1.78 to 1.56 for the Q&P steel grade. Similar results were obtained for the rest of the tested grades in the study [28]. To further confirm the two-point estimation of the CIDR, a comparison with the CIDR determined by a complete set of CI at different levels of intrusion was performed. To reduce the experimental spread and to obtain a better estimate, a series of 3 components was tested for each grade.

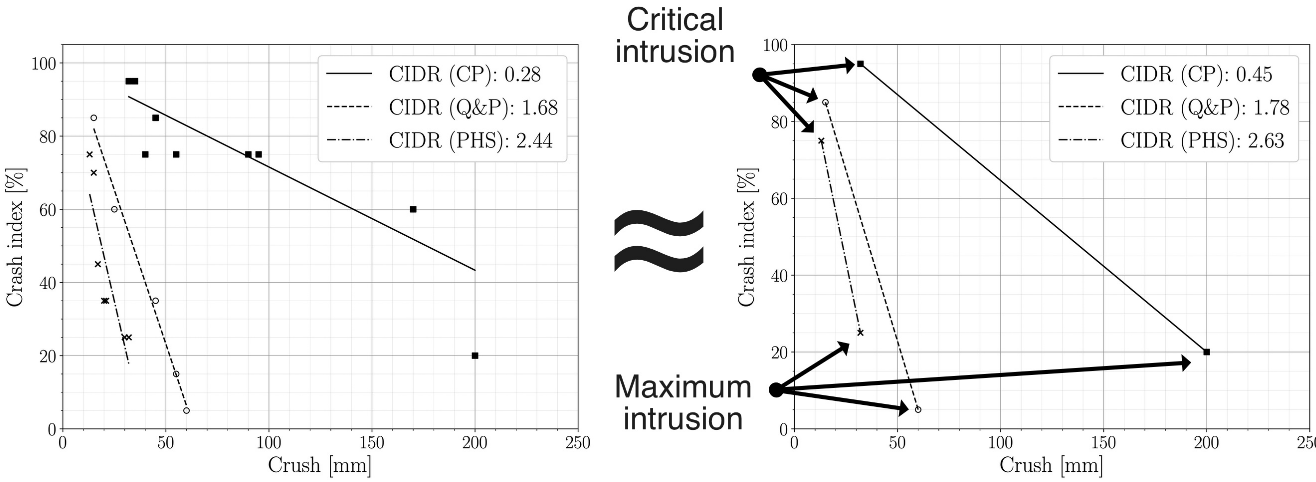

Figure 7. CIDR results estimated for three different steel grades from crash box experiments (**left**) and the proposed critical point method (**right**). Using the CI at critical intrusion (intrusion where the material starts to crack) and the CI at maximum intrusion, the CIDR can be estimated within engineering accuracy. Data adapted from Frómeta et al. [28]. Copyright (2019), with permission from Elsevier.

4. Finite Element Modelling

The aim of the numerical simulations was to validate the calibrated material and damage models by comparing the results from the axial compression experiments with the corresponding simulated outcome. The crash box experiments were modelled using FE software LS-DYNA® version R14 from LSTC (Ansys, Inc. Canonsburg, PA, USA). well known for its suitability for dynamic simulations due to its explicit time integration scheme. Since the crash box was precrushed by the manufacturer due to reasons explained earlier, an initial simulation was performed to reverse engineer the observed crush from the received boxes. The box was locked in position and deformed by a moving rigid plate, which first compressed the box followed by an unloading step. Due to the quasi-static conditions during the experimental precrushing, an implicit time integration scheme using fully integrated shell elements was utilised. An automatic single surface mortar contact was used, and the spot welds were simulated using tied contacts with a beam offset. The resulting geometry for the precrushed crash boxes compared with the real component can be seen in Figure 8.

For the high-speed simulation, a similar setup was used but instead of locking a node set, a load cell setup was used. The load cell was modelled as an elastic solid merged with a rigid contact plate, both with steel properties. The contact model used was of an automatic single surface type with a specified segment-based penalty contact formulation (SOFT = 2 in LS-DYNA®). A tied contact was used to represent the welds to the bottom plate at the end of the crash boxes. An explicit time integration scheme with fully integrated shell element formulation was used for the dynamic simulations with a shear scale factor of 5/6.

Figure 8. The precrushed crash boxes with FEM models. TBF 1180 to the left and PHS 1000 to the right.

4.1. Damage Modelling

A commercially available, generalised, incremental, stress-state-dependent damage model (GISSMO) [52–55] was chosen to introduce damage prediction capability into the FE analysis. Other authors have previously used this damage model to simulate wedge-bend, notched tensile, and axial crash tests of a 3rd-generation TRIP steel with promising results [56,57], and to predict fracture in the forming process of an alloy 718 at room temperature [58]. This model has also recently been used to predict the fracture behaviour of different microstructures in a PHS steel grade [59] by calculating the damage accumulation in each constituent. This model is well described in previously published papers [52–55,57] and consists of the following:

- A failure strain curve (for shells) defining the equivalent plastic strain to failure as a function of stress state (triaxiality). In this paper the plane stress isotropic von Mises MMC criterion defined in Equation (2) was used.
- The model consists of a incremental formulation of damage accumulation with a nonlinear damage evolution parameter ΔD of the Johnson–Cook type that evolves with the effective plastic strain at the initiation of the plastic deformation according to:

$$\Delta D = \frac{DMGEXP}{\varepsilon_f(\eta^*)} D^{(1-\frac{1}{DMGEXP})} \Delta\varepsilon^p \tag{5}$$

  This simple expression for damage accumulation takes the nonproportional loading into consideration. Here, the parameter DMGEXP needs to be calibrated using inverse modelling.
- A nonlinear material instability evolution parameter ΔF that evolves at the initiation of the plastic deformation in a similar manner as ΔD:

$$\Delta F = \frac{DMGEXP}{\varepsilon_i(\eta^*)} F^{(1-\frac{1}{DMGEXP})} \Delta\varepsilon^i \tag{6}$$

  The points of material instability is described with an instability curve, which is the critical plastic strain as a function of triaxiality. When F reaches unity, the damage parameter D is stored as the critical damage D_{crit}, and damage is then coupled to the stress tensor according to:

$$\sigma = \tilde{\sigma}\left[1 - \left(\frac{D - D_{crit}}{1 - D_{crit}}\right)^{FADEXP}\right] \tag{7}$$

  This reduces the strength of the material until the stress in the integration point is zero at $D = 1$. When the chosen number of integration points have failed, the damaged element is deleted. The fade out parameter FADEXP influences the softening response of the stress coupling.

The instability curve is, in general, triaxiality-dependent, sometimes calibrated using the equivalent plastic strain at diffuse necking in a Considére/Swift manner [60,61]. Some authors present this curve together with the failure locus [56,57] without further elaboration on how it was determined, while others use polynomial fitting to experimental data to obtain the curve, but leaving out the fitting parameters [33,58]. Since using an instability curve affects the failure prediction in simulations, a further rationale should be introduced to make it easier to adapt and compare them for different materials. One way is to use an instability model to predict material instability [61–65] or a forming limit diagram transformed into the space of effective plastic strain and triaxiality. In this article, a more pragmatic model was used, which was calibrated using tensile testing. Shear fractures are generally not preceded by diffuse necking, and thus, the curve should move asymptotically towards infinity for triaxialities equal to zero, similar to a multiplicative inverse expression with respect to triaxiality. The case with an instability close to the equi-biaxial triaxiality for sheet materials is a little trickier. However, it has been shown that the critical strain increases relative to the plane strain stress state at the equi-biaxial stress state [61,62], and thus, it is reasonable to assume that the curve increases after the plane strain triaxiality. Thus, adding an exponential term to the expression for the instability curve can be motivated. The following expression for the triaxiality-dependent instability curve was proposed:

$$\varepsilon_i(\eta) = \frac{a_i}{b_i\eta} + c_i e^{d_i\eta} \tag{8}$$

Equation (8) can then be calibrated by curve fitting using sheet tensile test geometries undergoing some diffuse necking, such as regular uniaxial tensile specimens or notched specimens, either together with the fracture strain predicted from the fitted failure locus or by the failure strain from equi-biaxial experiments. In this work, no equi-biaxial calibration (triaxiality of 0.66) testing was done, so it was assumed that the instability curve coincided with the failure curve at that stress state. The shape of the curve was similar to published curves [56,57] and was also easy to calibrate and easy to compare between materials, but it is important to note that this was a purely mathematical construct used to extrapolate the instability curve beyond the typical tensile tests for recreation purposes and was by no means intrinsic. Other authors have investigated material instability in more detail [61–65].

As mentioned, two parameters needed to be tuned: the damage exponent DMGEXP for nonlinear damage accumulation and the fade-out exponent FADEXP controlling the postnecking softening. This was performed using an inverse modelling of the straight tensile specimen at the maximum strain rate of 100 s^{-1}, since the crash boxes were tested at high speeds. The used damage model was limited to a constant damage exponent for all triaxialities, which is a simplification since it can differ for different stress states for some materials [66].

4.2. Discretisation and Meshing

One problem in modelling fracture, regardless of element formulation, is the possible mesh dependence of the postinstability solutions [67]. The calibrated length scale for the calibration tensile tests using DIC was approximated to 0.1 mm, a mesh size too small to get reasonable computation times for the larger crash boxes. The damage model was therefore scaled to the larger mesh size of 1 mm. The straight tensile test ($\eta = 0.33$) was used as the foundation for regularisation to scale the fracture strain. However, it is important to note this scaling factor is not necessarily constant for all triaxialities. Earlier inverse modelling work on simulation of 3rd-generations AHSS has shown that the shear stress state was well captured using no regularisation [56]. This is plausible since the shear fractures are rarely preceded by necking as mentioned above. The equi-biaxial stress state is more complicated, where some authors present good results when simulating equi-biaxial punch loading with full regularisation (same scaling factor as for uniaxial tension) [56], while results by other authors suggest a low mesh sensitivity for this stress state, at least for cases where the sheet structure is larger than the sheet thickness [68,69]. In this work, no mesh regularisation (no fracture strain scaling) was chosen for either the shear or equi-biaxial stress state. The scaling factor between these three triaxialities are interpolated linearly.

4.3. Validation

The validation of damage models is often conducted by comparing the final state of the simulation with the postexperimental results of the tested components. Here, the validation step was expanded by taking the evolution of the damage into account. The crash index evolution technique used for the experiments in Figure 6 was therefore also used to investigate the selected damage evolution model in the FE analysis. By measuring the coherent array of deleted elements as a "crack", the evolution of the damage can be tracked with the crushing depth during simulation. The authors are aware of the fact that the deleted elements from a ductile damage model are not real cracks, but it does allow the study of the evolution of the damage for a more extensive comparison with experiments. This is in contrast to just comparing the resulting damage after the maximum crushing distance after the experiment. The 3D-DIC method also allows for a direct comparison of strain fields between the FEM and the experiment.

5. Results and Discussion

5.1. Tensile Tests

Tensile testing results for quasi-static and high-loading-rate conditions are presented in Figure 9 for the TBF 1180 steel grade (left) and the PHS 1000 steel grade (right). The elongation, A50 mm, was larger for the TBF 1180 steel grade than for the PHS 1000 grade, and that elongation increased with the increased strain rate for the TBF 1180 steel grade while no clear trend for the PHS 1000 steel grade was found. A similar behaviour with an increasing elongation with the strain rate for the TBF 1180 grade was found in other works [18] and was suggested to be related to the austenite stability relative to the strain. The ultimate tensile strength (UTS) and 0.2% offset yield (YS) at the different strain rates are summarised in Tables 3 and 4. The results show a slight trend towards higher UTSs and offset yields with the increasing strain rate with the exception of the quasi-static yield strength for the TBF 1180 steel grade and the UTS for the PHS 1000 steel grade. Overall, the strain rate effect on plasticity was not significant for either steel grade tested.

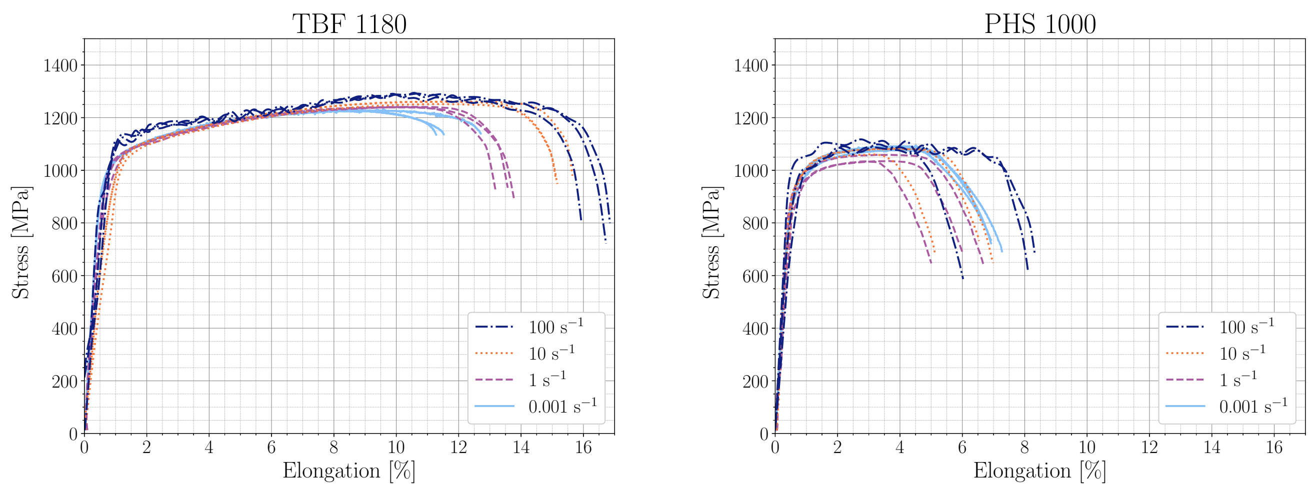

Figure 9. Engineering stress versus elongation curves for the TBF 1180 grade (**left**) and PHS 1000 grade (**right**) for the strain rates of 0.001 s^{-1}, 1 s^{-1}, 10 s^{-1}, and 100 s^{-1}.

Table 3. Tensile testing results (mean values from 3 experiments together with minimum and maximum experimental values in parenthesis) for different strain rates for the TBF 1180 steel grade. YS is the offset yield point and UTS is the ultimate tensile strength. The elongation to fracture was measured in L50 specimens (A50).

TBF 1180 (1.4 mm Thickness)			
$\dot{\varepsilon}$ (s^{-1})	YS (Min/Max) (MPa)	UTS (Min/Max) (MPa)	Elongation (Min/Max) (%)
0.001	983 (979/985)	1232 (1230/1234)	11.8 (11.3/12.7)
1	951 (893/987)	1240 (1239/1241)	13.5 (13.2/13.8)
10	1008 (987/1028)	1258 (1252/1262)	15.3 (15.1/15.7)
100	1035 (966/1076)	1291 (1287/1294)	16.5 (15.9/16.9)

Table 4. Tensile testing results (mean values from 3 experiments together with minimum and maximum experimental values in parenthesis) for different strain rates for the PHS 1000 steel grade. YS is the offset yield point and UTS is the ultimate tensile strength. The elongation to fracture was measured in L50 specimens (A50).

PHS 1000 (1.55 mm Thickness)			
$\dot{\varepsilon}$ (s^{-1})	YS (Min/Max) (MPa)	UTS (Min/Max) (MPa)	Elongation (Min/Max) (%)
0.001	926 (907/942)	1087 (1080/1095)	7.0 (6.9/7.3)
1	931 (916/948)	1043 (1034/1059)	5.9 (5.0/6.7)
10	955 (951/960)	1075 (1061/1082)	6.2 (5.1/7.0)
100	1005 (987/1035)	1104 (1094/1118)	7.5 (6.0/8.3)

5.2. Constitutive Modelling

The flow stress curves obtained from applying the isotropic version of SMM on the notched R3.75 geometry are presented in Figure 2. The results for the two grades are presented in Figure 10 together with curves based on the simplified Johnson–Cook model with calibrated parameters. The TBF 1180 grade shows a larger strain hardening compared to the PHS 1000 steel grade.

5.3. Fracture Criterion and Damage Model

The calibrated instability curves according to Equation (8) are presented in Figure 11. The results show a low value of effective plastic strains for the PHS 1000 grade with slightly larger values for the uniaxial tensile stress state than for the notched specimens (biaxial stress states). A similar trend is seen for the TBF 1180 grade but with larger values across the board for the effective plastic strains at diffuse necking. The damage is thus coupled to the stress tensor earlier for the PHS 1000 grade than for the TBF 1180 grade in the damage model. Furthermore, no clear strain rate dependency can be seen for the investigated strain rates for either of the grades regarding instability.

The calibrated MMC failure curves are presented in Figure 12 with the plot interval beginning at the cutoff value of the triaxiality value -0.33 in accordance with previously published work by other authors [41]. The scatter points represent the integrated average triaxiality from Equation (4) for the different tensile geometries used for the curve-fitting procedure. The local ductilities for the shear stress and the uniaxial tensile stress state are significantly higher for the PHS 1000 grade compared to the TBF 1180 grade.

Comparing the failure curves in Figure 12 with the results from the uniaxial tensile tests in Figure 9 show that although the global ductility (total elongation) is significantly lower for the PHS 1000 steel grade compared to the TBF 1180 steel grade, the local ductility acquired from full-field measurements is a lot higher for the PHS 1000 grade. Hence, the global ductility measured using regular tensile tests is not synonymous with a good local ductility, something which has been previously stated by other authors as well [16,17,70].

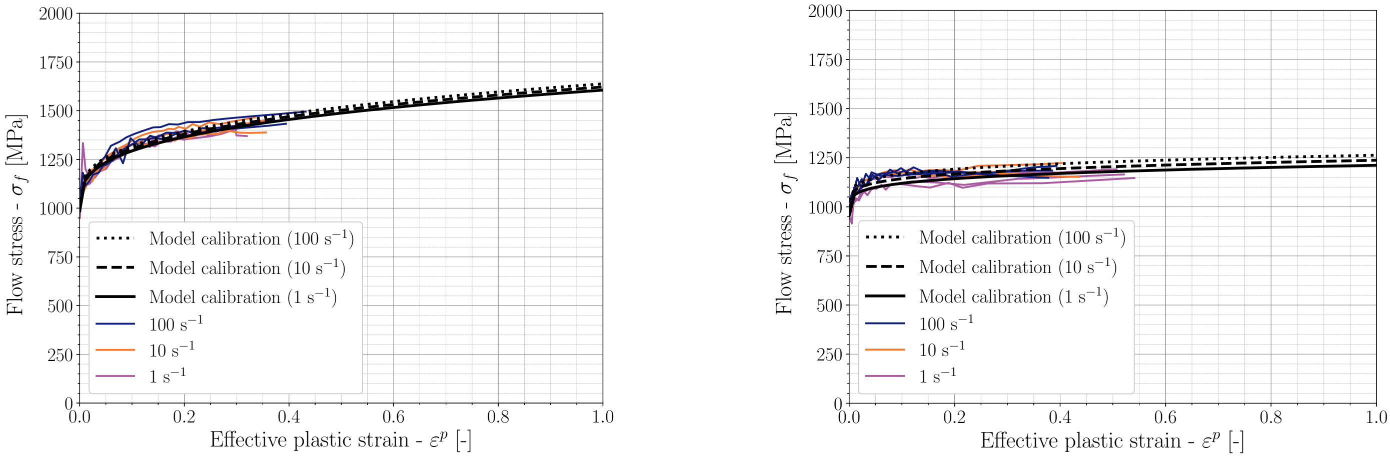

Johnson–Cook parameters (TBF 1180)			
A (MPa)	B (MPa)	n (-)	C (-)
$9.86 \cdot 10^2$	$6.20 \cdot 10^2$	$3.04 \cdot 10^{-1}$	$4.37 \cdot 10^{-3}$

Johnson–Cook parameters (PHS 1000)			
A (MPa)	B (MPa)	n (-)	C (-)
$9.55 \cdot 10^2$	$2.56 \cdot 10^2$	$1.92 \cdot 10^{-1}$	$9.19 \cdot 10^{-3}$

Figure 10. The calculated flow curves from the stepwise modelling for three different strain rates as well as the fitted Johnson—Cook flow curves together with the parameters used for the simulations. To the left is the TBF 1180 steel grade and to the right is the PHS 1000 steel grade.

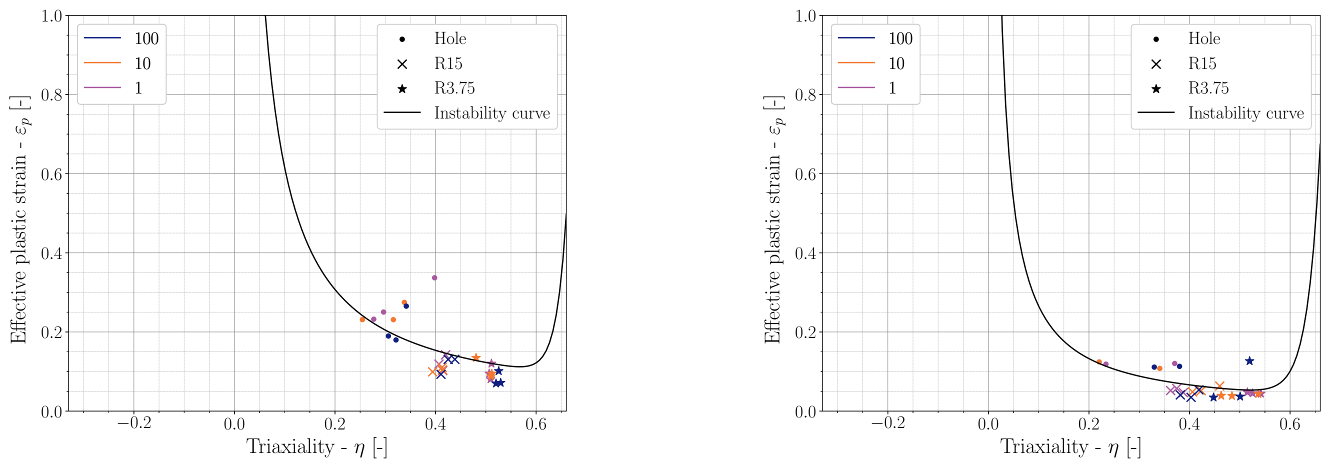

Instability curve parameters (TBF 1180)			
a_i (-)	b_i (-)	c_i (-)	d_i (-)
$1.16 \cdot 10^{-1}$	$1.88 \cdot 10^0$	$1.31 \cdot 10^{-15}$	$5.06 \cdot 10^1$

Instability curve parameters (PHS 1000)			
a_i (-)	b_i (-)	c_i (-)	d_i (-)
$2.24 \cdot 10^{-2}$	$8.43 \cdot 10^{-1}$	$1.75 \cdot 10^{-12}$	$4.03 \cdot 10^1$

Figure 11. The fitted parameters for the instability curve in Equation (2) using average triaxiality values for local plastic strains at maximum load. To the left is the TBF 1180 steel grade and to the right is the PHS 1000 steel grade.

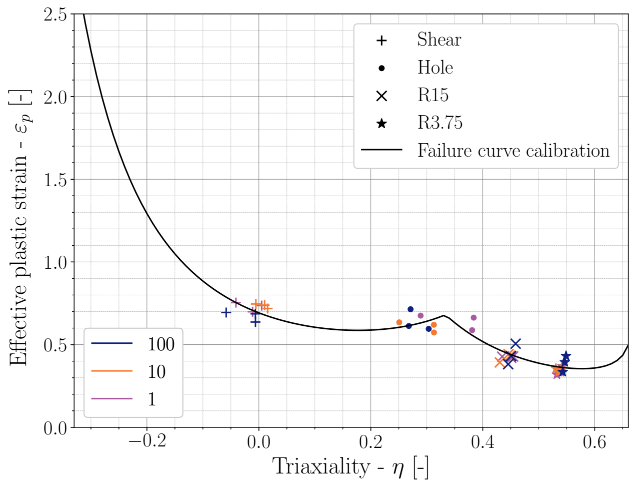

Failure curve parameters (TBF 1180)			
A (MPa) *	c_1 (-)	c_2 [MPa]	n (-)
$9.86 \cdot 10^2$	$1.61 \cdot 10^{-1}$	$5.32 \cdot 10^2$	$2.21 \cdot 10^{-1}$

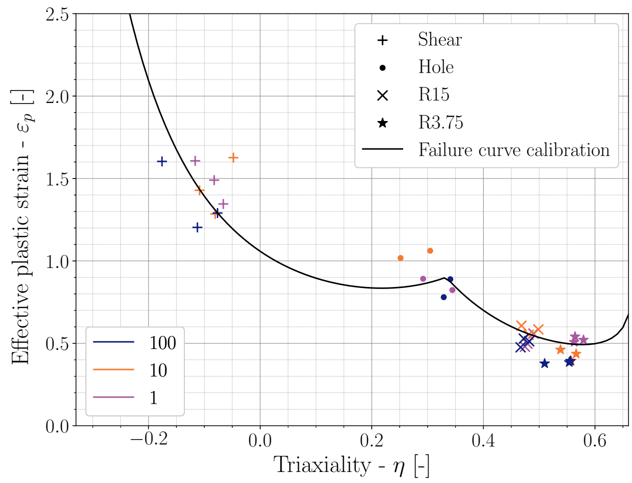

Failure curve parameters (PHS 1000)			
A (MPa) *	c_1 (-)	c_2 (MPa)	n (-)
$9.55 \cdot 10^2$	$2.38 \cdot 10^{-1}$	$5.70 \cdot 10^2$	$2.04 \cdot 10^{-1}$

Figure 12. Fitted parameters for the plane-stress MMC failure curve with the von Mises yield function presented in Equation (2) using average triaxiality values. To the left is the TBF 1180 steel grade and to the right is the PHS 1000 steel grade. *: value taken from Figure 10.

5.4. Axial Compression Experiments

Results in terms of load vs. crush curves for the high-speed axial compression experiments for the TBF 1180 crash boxes are presented in Figure 13. The curves were filtered with a CFC1000 (ISO-6487) filter [71] to reduce noise. The precrushed boxes effectively lowered the initial load peak which could otherwise be significantly higher. Summarising the results in Table 5, it is obvious that the spread is large between the experiments for all the measured quantities. The energy absorbed is the cumulative integration of the load response. The results for the PHS 1000 crash boxes are presented in Figure 14 and summarised in Table 6. In contrast to the TBF 1180 grade, results are similar for all experiments with a low spread for all the measured quantities. The intrusion and the intrusion speed were lower for this crash box setup, while the average force was higher. It should be highlighted that a direct comparison of the performance for the two grades should not be conducted due to the different crash box geometries.

Table 5. Results from the TBF 1180 crash box experiments presented in Figure 13.

	TBF 1180					
	Absorbed Energy (kJ)	Maximum Force (kN)	Average Force (kN)	Crush (mm)	Maximum Crush Speed (ms^{-1})	Average Crush Speed (ms^{-1})
#1	15.5	163	101	154	20.2	16.1
#2	14.0	188	80	165	23.1	14.1
#3	11.1	153	89	131	22.3	13.2
Mean	13.5	168	90	150	21.0	14.5

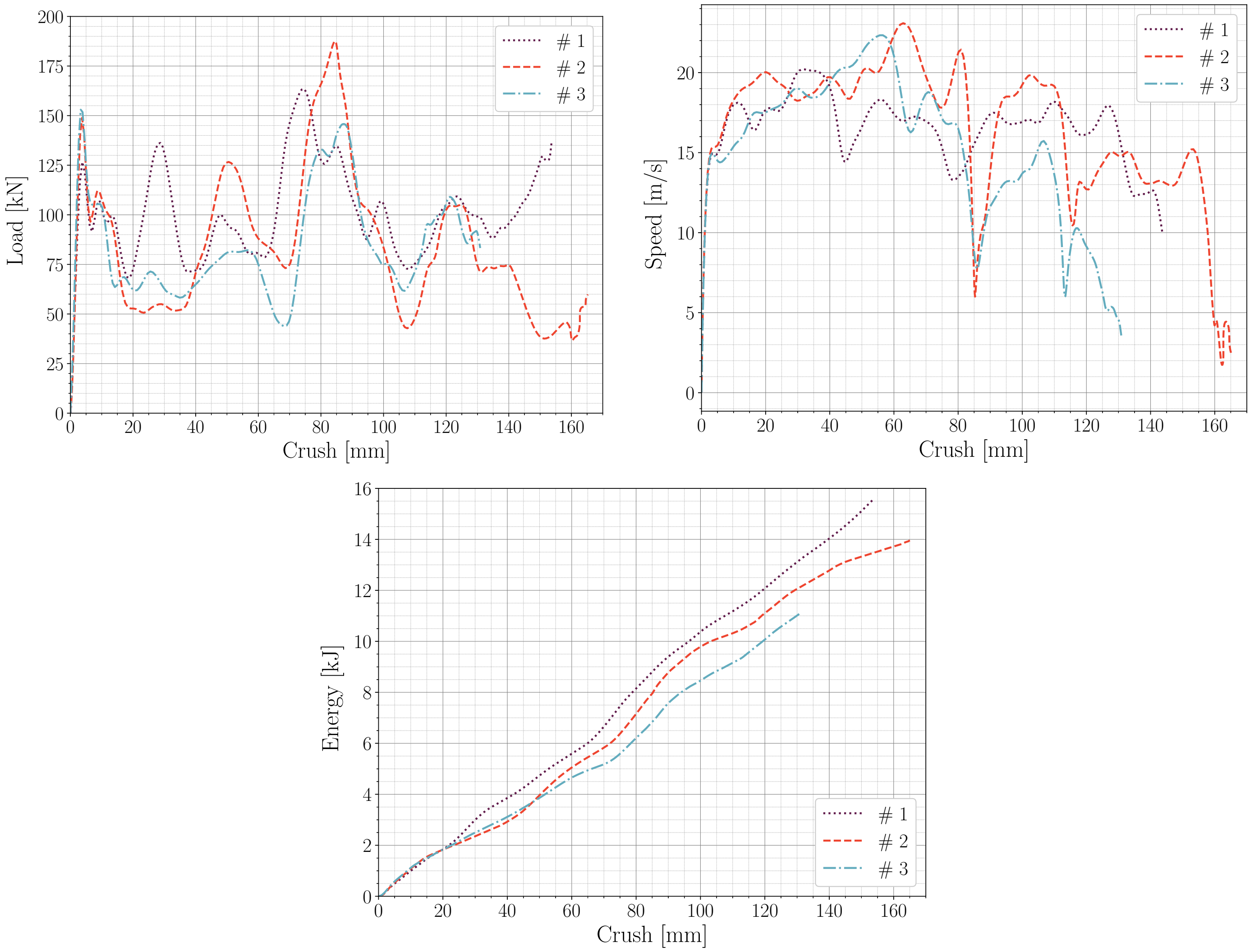

Figure 13. The load response (**top left**), crush-speed evolution (**top right**), and energy absorption (**bottom**) for the predeformed TBF 1180 crash boxes as a function of crushing distance. The results were filtered using a CFC1000 filter (ISO-6487).

Table 6. Results from the PHS 1000 crash box experiments presented in Figure 14.

	PHS 1000					
	Absorbed Energy (kJ)	**Maximum Force (kN)**	**Average Force (kN)**	**Crush (mm)**	**Maximum Crush Speed (ms^{-1})**	**Average Crush Speed (ms^{-1})**
#1	11.3	182	93	121	19.3	12.1
#2	11.5	176	96	117	21.0	12.2
#3	11.1	184	108	110	19.7	13.4
Mean	11.3	181	99	116	20.0	12.6

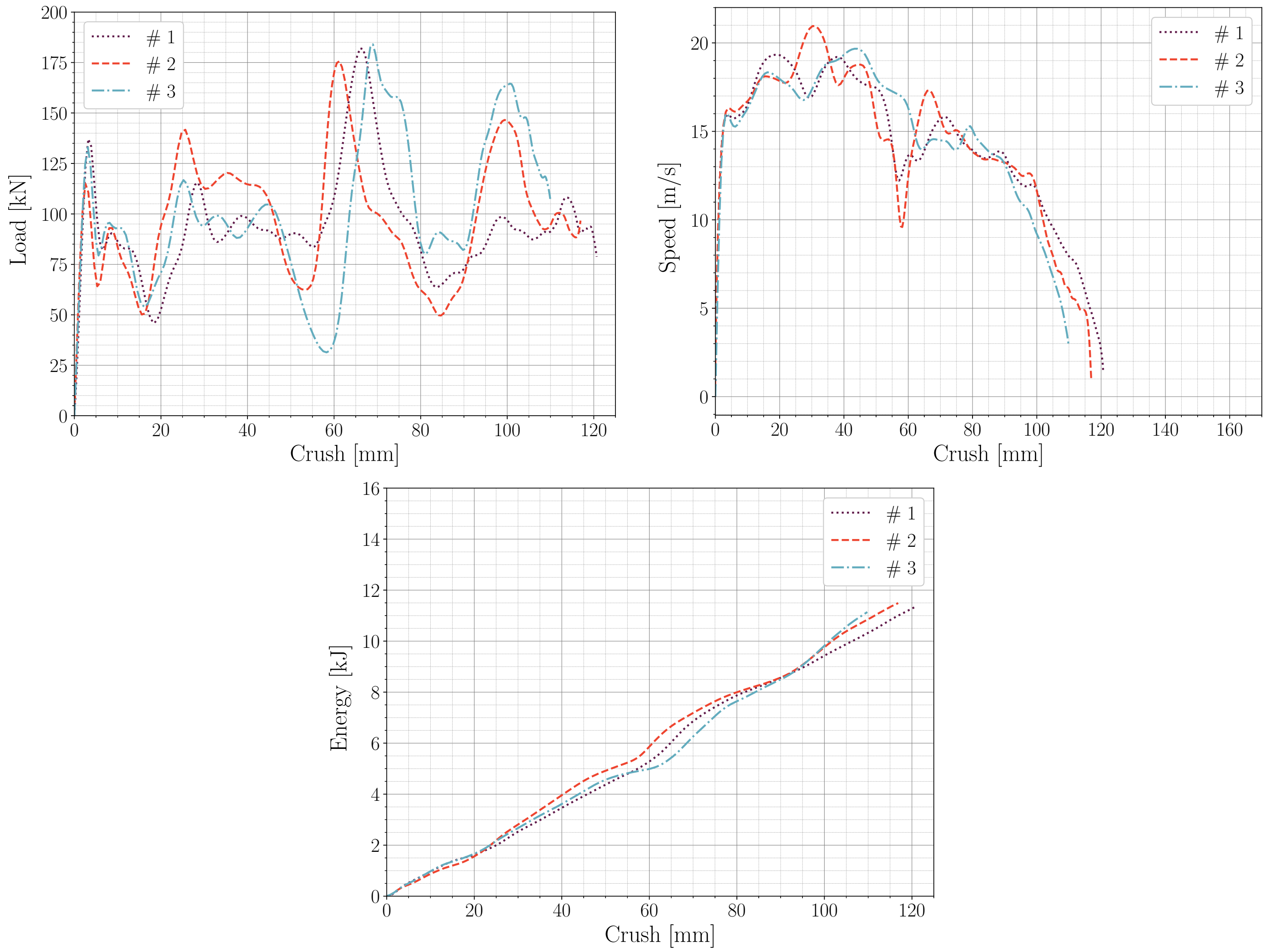

Figure 14. The load response (**top left**), crush-speed evolution (**top right**), and energy absorption (**bottom**) for the predeformed PHS 1000 crash boxes as a function of crushing distance. The results were filtered using a CFC1000 filter (ISO-6487).

5.5. Crashworthiness Evaluation

The main benefit of using high-speed imaging in crash box evaluation is the ability to track the evolution of damage during the entire deformation process. This makes it possible to identify where cracks initiate and how they propagate during the crushing of the crash box. An example of the methodology can be seen in Figure 15 where the crushing distance as a function of time is presented for a couple of the TBF 1180 crash boxes along with images showing some of the crack initiation sites in the bulk materials as well as spot-weld fractures. The images in Figure 16 show the locations of typical cracks in the TBF 1180 crash boxes after maximum crushing distance. Depending on the initiation cause, the damage could vary significantly, which can explain the large spread in the results for the energy absorption, loads, and crushing distances. Cracks in the bulk materials generally appeared in the folds, while tearing behaviour could be seen in the flange areas from failures around spot welds. Figure 17 shows the locations of typical cracks in the PHS 1000 crash boxes after maximum crushing distance. Compared to the TBF 1180 results, cracking was significantly lower for these crash boxes. Spot weld unbuttoning was present but had a lesser impact on the results, and the folding behaviour was generally better. This explains the narrow spread between the experiments for the PHS 1000 crash box setup. Cracks were generally located underneath the folds for the PHS 1000 crash boxes.

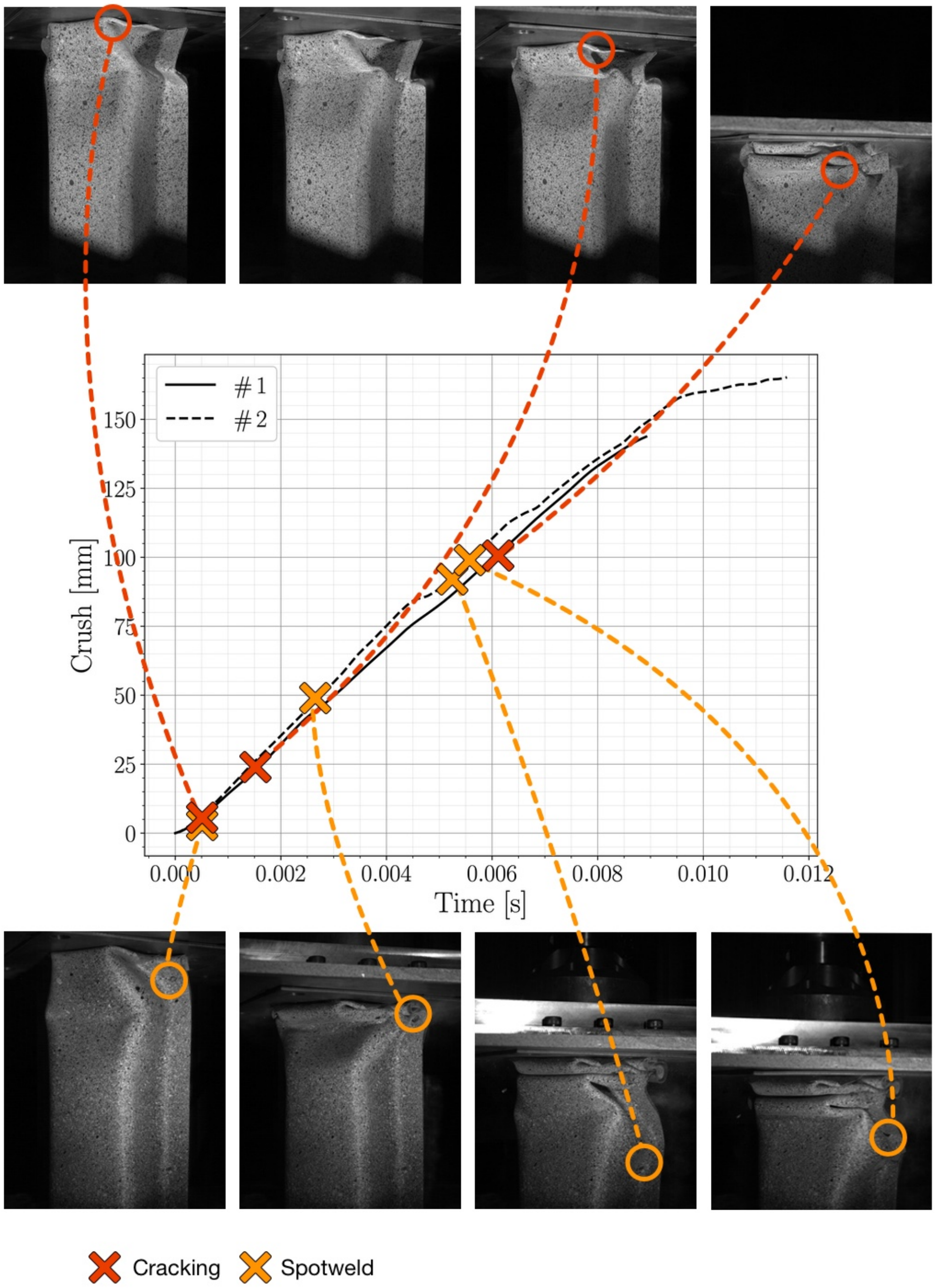

Figure 15. Crushing distance over time for two TBF 1180 crash boxes under axial compression. A distinction can be made between bulk material cracking and spot-weld fractures during the deformation process.

In order to quantify the crash performance of the crash boxes, the CIDR was revisited using the 3D-DIC setup to detect when cracks appeared during the crush. Two measures to estimate the CIDR were compared. The first measure was based on the two critical points (critical intrusion point and maximum intrusion point), and the second was based on a complete set of intrusion levels. The CIDR for each grade are presented in Figure 18, using three boxes for TBF 1180 and four boxes for PHS 1000 (due to the lack of visible cracks, an extra crash box was used for CIDR evaluation). In the left figure for TBF 1180, the solid line represents the measure based on a complete set, whereas the dashed line represent the critical-point method. However, for PHS 1000, no complete set could be obtained, and therefore, only the latter measure is presented. The two estimates of CIDR gave the same CIDR, 0.43, for TFB 1180 crash boxes. The CIDR for the PHS 1000 crash boxes became 0.23 due to less cracking.

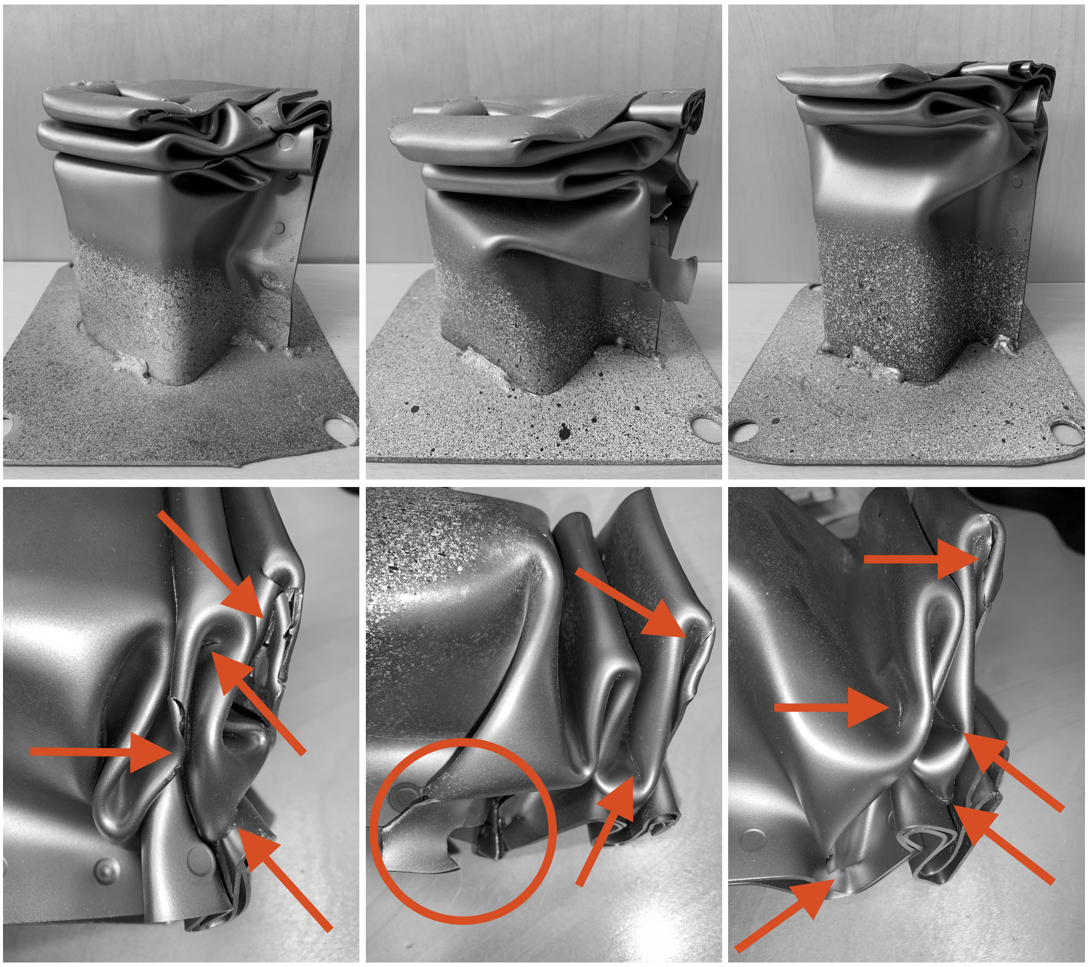

Figure 16. Some examples of locations of cracks for the TBF 1180 crash box after axial compression.

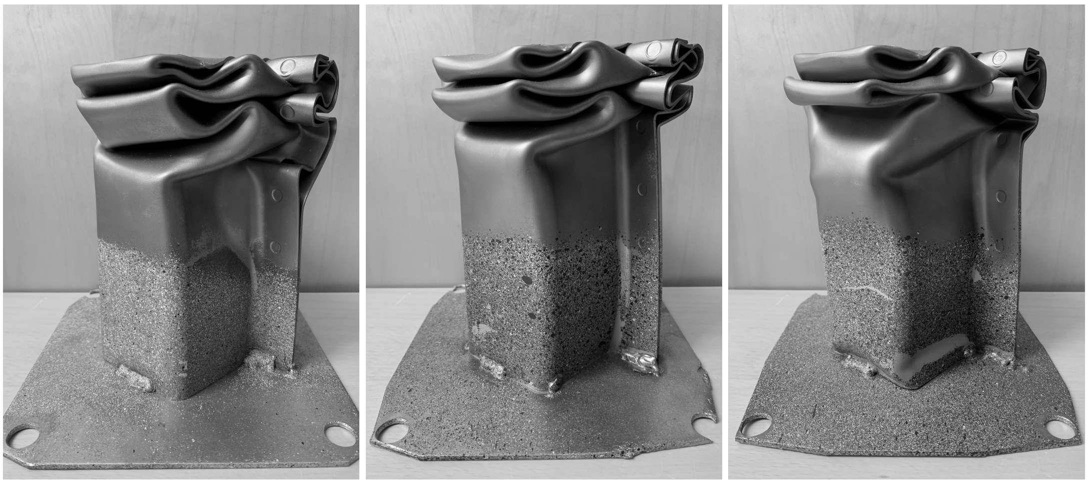

Figure 17. *Cont.*

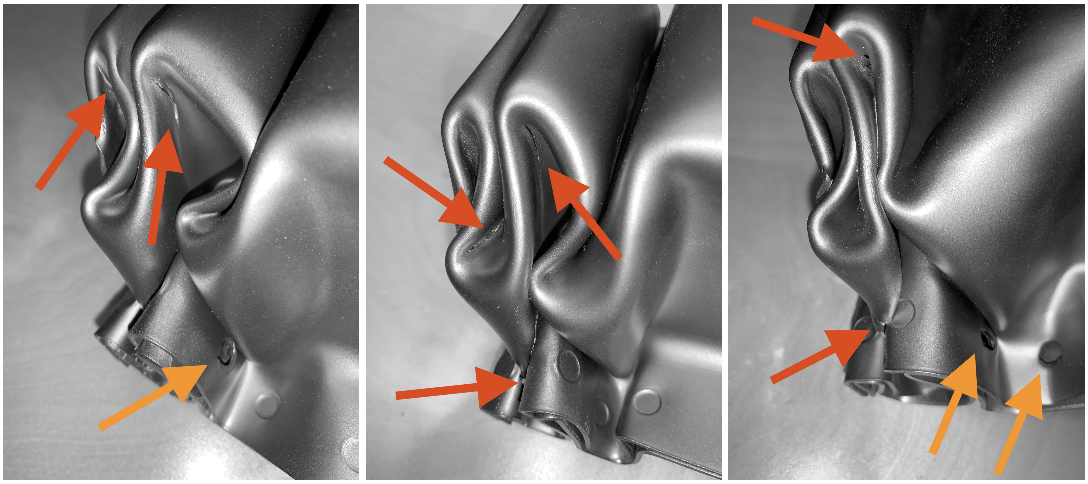

Figure 17. Some examples of locations of cracks for the PHS 1000 crash box after axial compression. Cracking was generally located underneath the folds. Red arrows show cracks in the bulk material while orange arrows show unbuttoned spot welds.

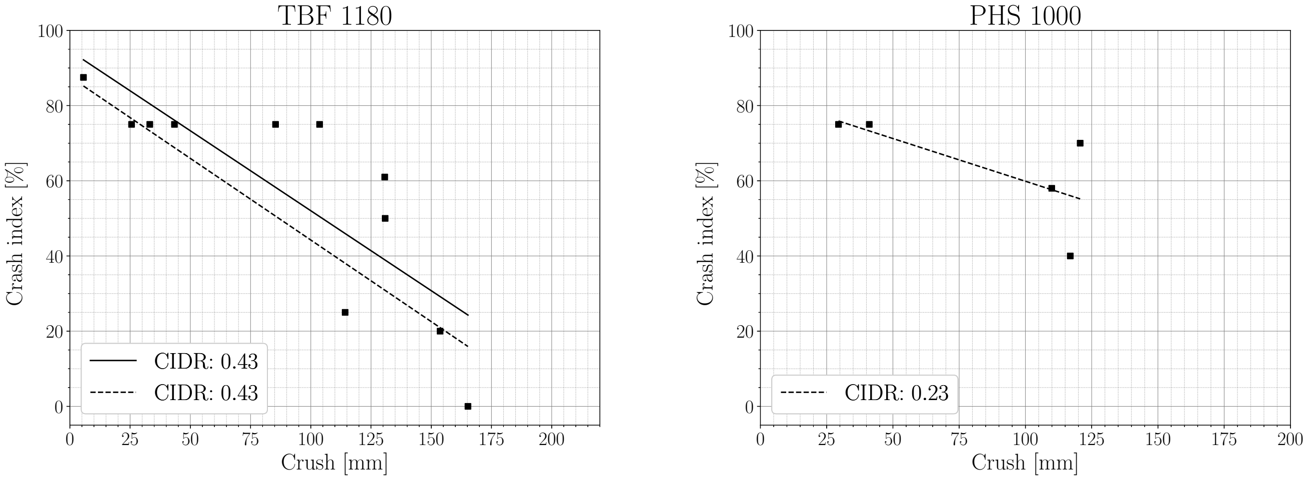

Figure 18. CIDR for the TBF 1180 crash box and PHS 1000 crash box estimated from high-speed imaging and postexperiment evaluation. The solid line represents the CIDR determined from the complete set of cracks detected, while the dashed line show CIDR estimated by the proposed critical point method.

5.6. Finite Element Analysis

5.6.1. TBF 1180 Simulation Results

To investigate the global crashworthiness behaviour of the TBF 1180, crash box simulations were performed. The load response and energy absorption are presented in Figure 19. The peak loads at folding were not accurately captured, but the average level is in relatively good agreement. The total energy absorption is similar to experiments, only underestimating it by approximately 1 kJ. It is worth mentioning that the later stages of the simulations of axial compression might be strongly influenced by the contact formulation used, and thus the results might depend on more than the material and damage model.

The damage prediction at maximum crush distance and the damage evolution prediction for the FEM model compared to the experimentally determined CIDR is presented in Figure 20. In the left image, the positions of the predicted cracks are highlighted on the origin geometry. The ductile damage model predicted the critical intrusion and the maximal crush damage reasonably well, but the damage evolution was not accurately captured. Damage grows quickly after critical intrusion to maximum damage in a power-law manner in contrast to the more linear behaviour seen in this study and previously published results [28]. Thus, a power-law fit is presented in Figure 20 for the simulated results instead of a linear fit. The predicted damage for the FEM model after crush is depicted at the bottom figure (compare with Figure 16).

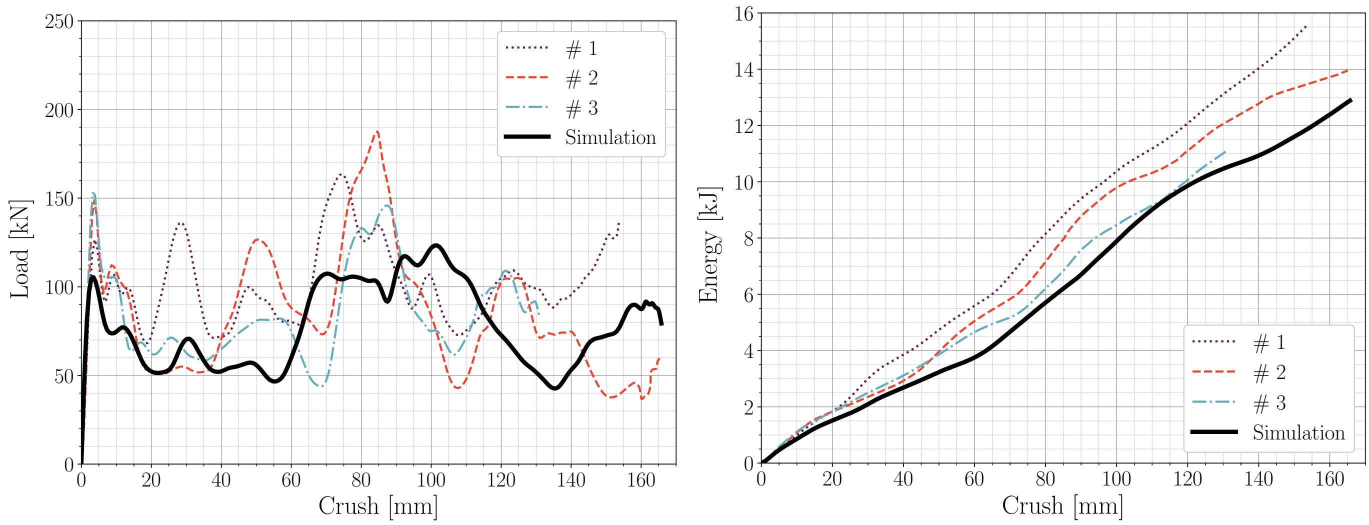

Figure 19. The simulated load response together with the experimental results (**left**) and energy absorption (**right**) for the predeformed TBF 1180 crash boxes as a function of crushing distance.

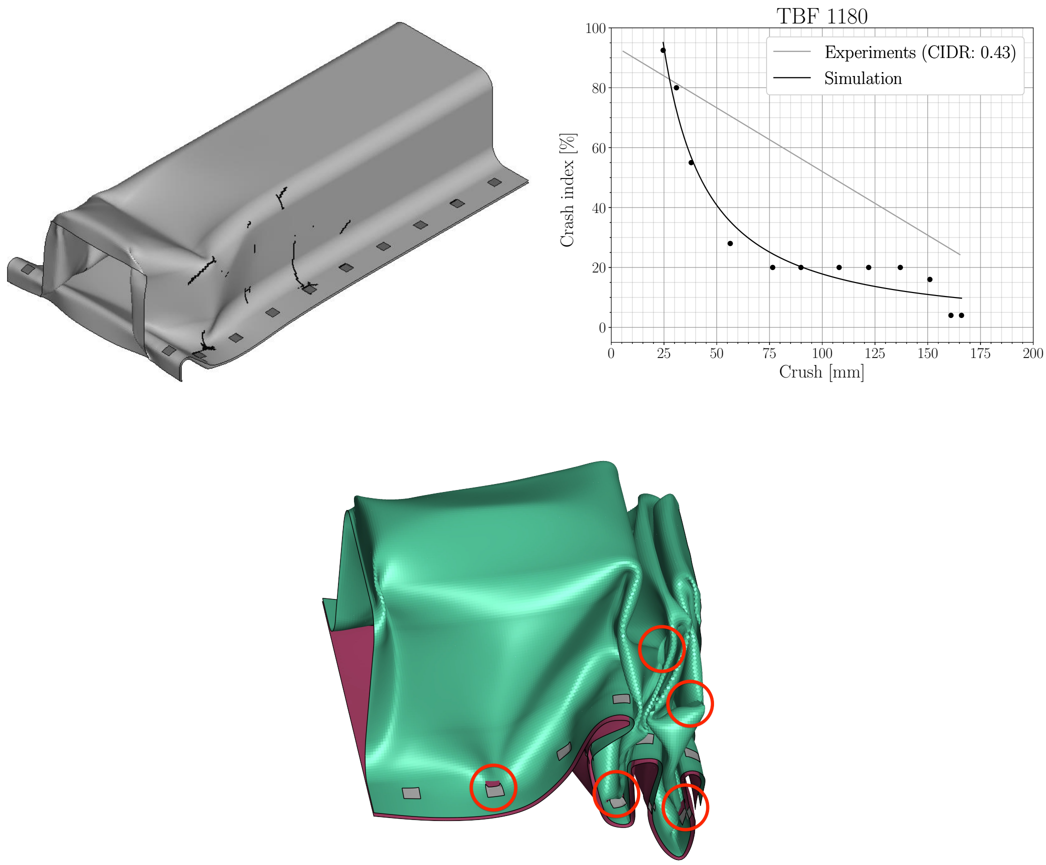

Figure 20. CIDR evaluation for the TBF 1180 crash box simulation compared with experiments. The left image shows the deleted elements after the maximum crush distance (origin geometry) in the FEM model, and the right image shows the simulated damage evolution (power law) compared to the experimentally determined CIDR (linear). The bottom image shows the FEM model after crush with the damaged areas.

For a more direct comparison between simulation and experiments, raw images, 3D-DIC results, and FEM results are presented in Figure 21 for three crushing depths. The legend shows the von Mises effective strain and is capped at 0.25 to make the comparison easier. The FE analysis results are similar to the 3D-DIC results at these lower crushing distances. At larger crushing distances, the DIC algorithm had a correlation problem due to the loss of facets necessary to capture the strains. However, despite missing information regarding the strain at certain regions, the remaining data together with the FE simulations are still valuable for a postanalysis of the experiment. Qualitatively, the strain measurements from the FE results matched well with the experimentally measured values, and 3D-DIC offered interesting validation possibilities to identify high-risk areas in a component.

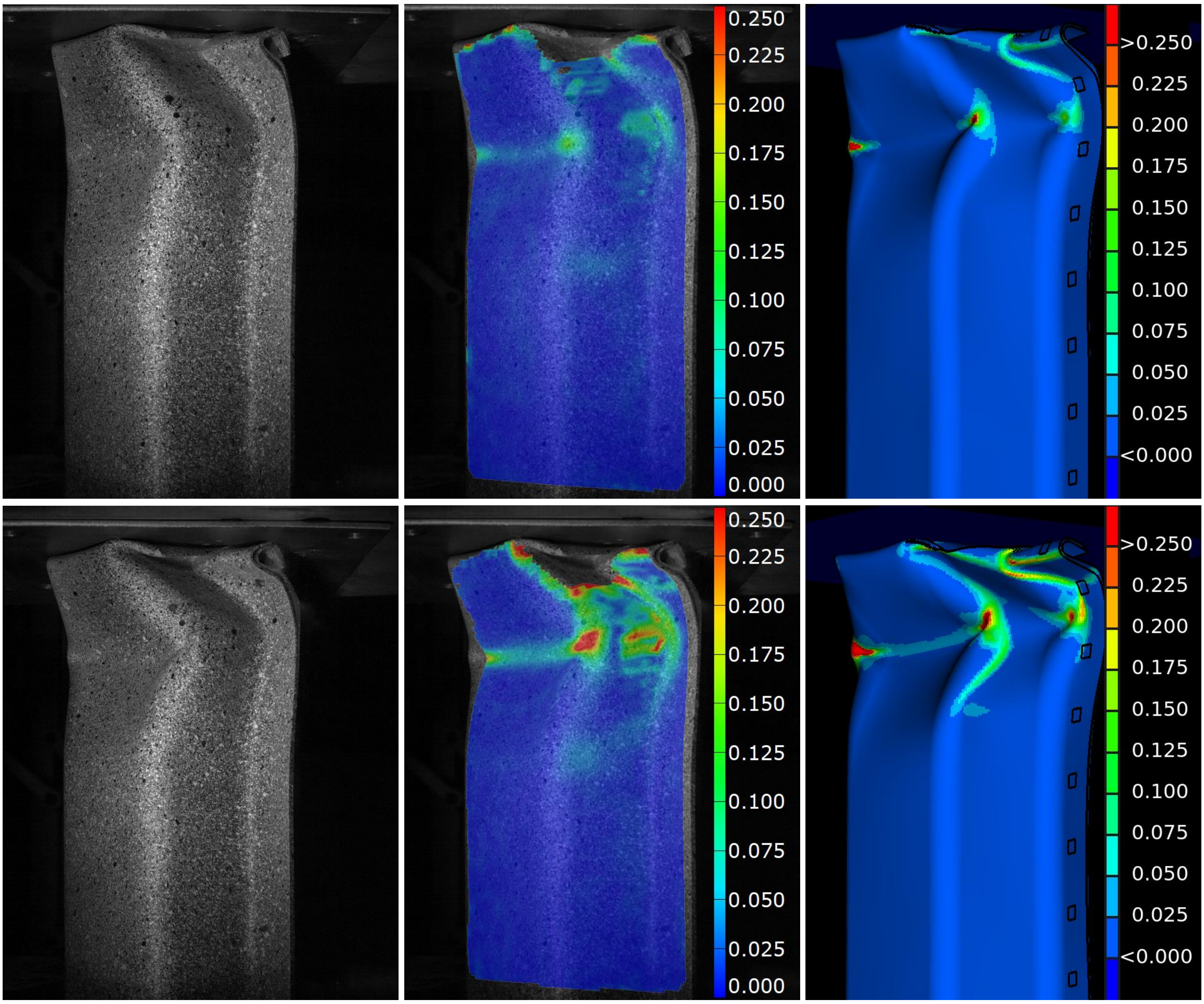

Figure 21. *Cont.*

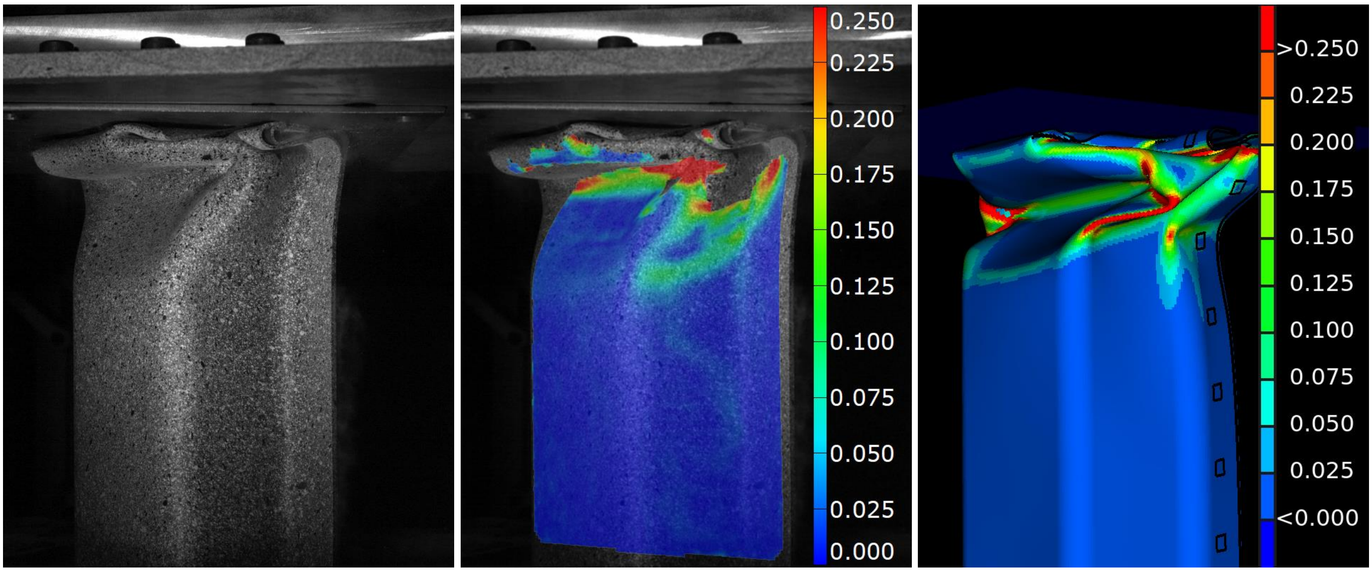

Figure 21. A comparison between raw images, 3D digital image correlation, and FE simulation results for three different crush depths for the TBF 1180 crash box. The legend shows the effective strain.

5.6.2. PHS 1000

The load response and energy absorption of the simulation results for the PHS 1000 crash box is presented in Figure 22. The folding behaviour was captured nicely, both the initial peak and the subsequent peaks, except for the third peak at a crush of approximately 70 mm. Hence, the energy absorption followed the experiments accurately as well, at least to the third peak. Due to the underestimation of this peak, the total energy absorption was underestimated by 1.7 kJ for the FE analysis. The crash index evolution for the PHS 1000 crash box simulations is presented in Figure 23 along with the predicted damage for the FEM model after crush (compare with Figure 17). Although the critical intrusion was captured reasonably well, the maximum damage was slightly overestimated compared to experiments. In contrast to the TBF 1180 results, a linear fit matched the results well, but the crash index deteriorated faster than estimated from the experiments (0.80 compared to 0.23). Due to the low number of experimental evaluation points for the PHS 1000, this result should be seen as a rough estimate and no strong conclusions can generally be made. The trend was, however, similar to the TBF 1180 results where the damage evolution measured in terms of deterioration of CI was overestimated for the FEM model used. The overall lower predicted damage at maximum intrusion is not surprising due to the larger local ductility measured for PHS 1000 compared to TBF 1180 Figure 12. Furthermore, Figure 24 shows the 3D-DIC results for a PHS 1000 crash box for three different crushing depths. As for the TBF 1180 crash box, a simulation without the mapped strain from the precrush simulations was used for comparison with the DIC. The effective von Mises strain from the simulation agreed quite well with the FE results.

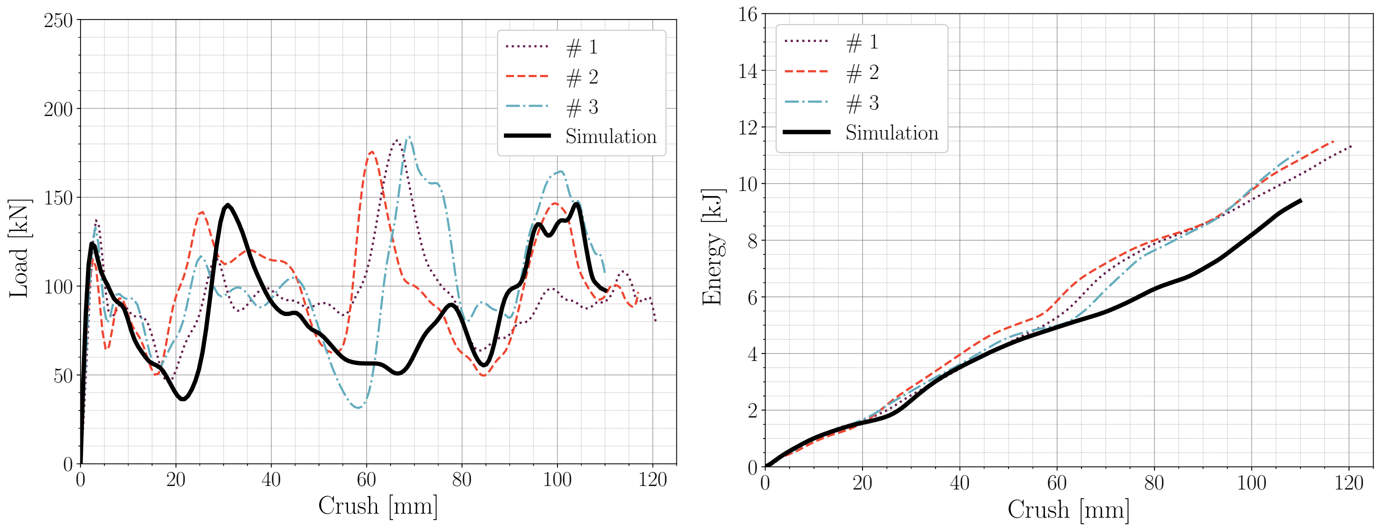

Figure 22. The simulated load response together with the experimental results (**left**) and energy absorption (**right**) for the predeformed PHS 1000 crash boxes as a function of crushing distance.

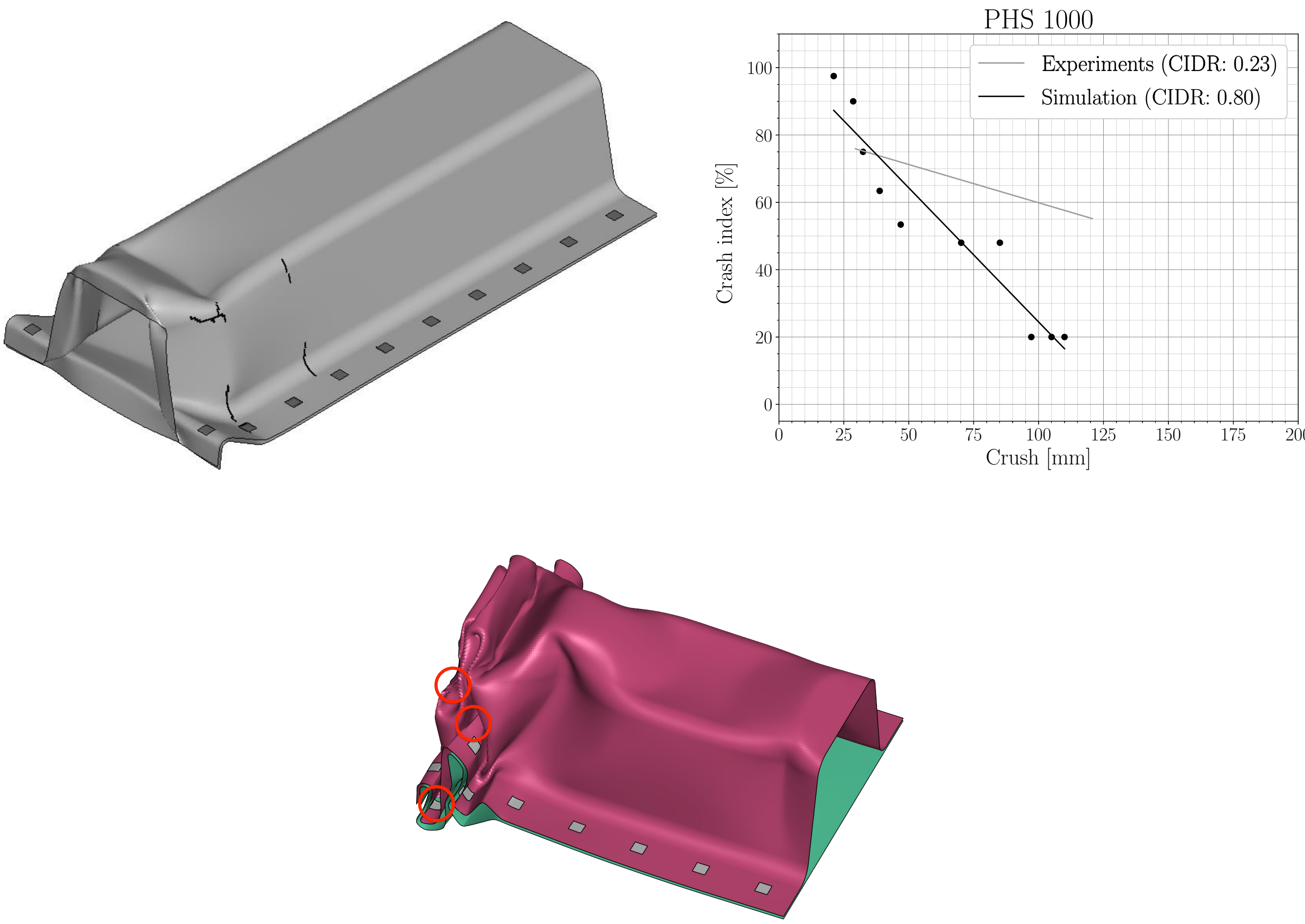

Figure 23. CIDR evaluation for the PHS 1000 crash box simulation compared with the experiments. The left image shows the deleted elements after the maximum crush distance (origin geometry) in the FEM model, and the right image shows the simulated damage evolution (power law) compared to the experimentally determined CIDR (linear). The bottom image shows the FEM model after crush with the damaged areas.

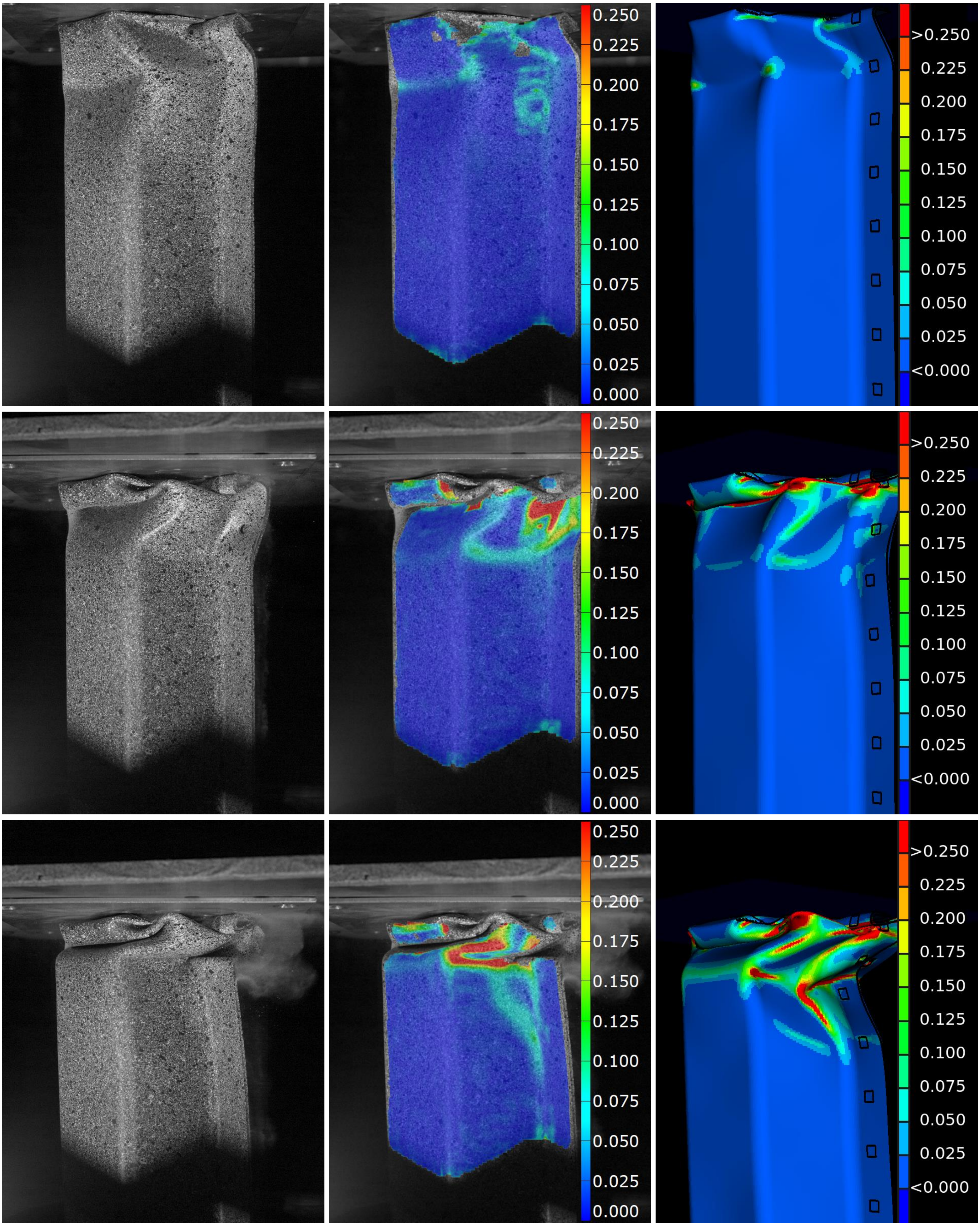

Figure 24. A comparison between raw images, 3D digital image correlation, and FE simulation results for three different crushing distances for the PHS 1000 crash box. The legend shows the effective strain.

6. General Discussion

There are some challenges when using a crash index to rate materials in terms of crashworthiness. The geometry of the boxes and settings during testing must be the same when comparing different materials. Furthermore, measuring cracks is not straightforward. The postmeasurement of cracks can generally be performed with a high accuracy if the cracks are not inconspicuous. Causes of crack initiations are, however, not captured using postmeasurements. High-speed imaging is a powerful tool here, but precise measurements of lengths are more difficult to make, and sometimes estimates have to be made.

The cause of the discrepancies between experiments and simulation in the energy absorption is hard to identify. It was clear from experiments, however, that spot-weld fractures were common. A simplified contact-based spot-weld formulation was used, which might not necessarily describe the reality that well. Fractured spot welds change the load state significantly, and to mimic the entire deformation process is very difficult. Recently published studies of hybrid double-hat profiles also showed some discrepancy between simulation and experiments beyond displacements of 60 mm, in this case due to more a complex and unstable behaviour caused by a failure of adhesive bonding [72].

For both tested steel grades, it is clear that the selected ductile damage model, GISSMO with the failure criterion MMC, overestimated the damage evolution, causing a higher CIDR compared to the rates estimated experimentally. Because of the challenges of predicting crack initiations and the subsequent growth, the intrinsic material property, fracture toughness, may be used to evaluate crashworthiness. Frómeta et al. [28] have shown good correlation between fracture toughness and crash resistance for AHSS:s. The fracture toughness for sheet metals were effectively evaluated using the essential work of fracture (EWF) [73,74]. This technique focuses only on the bulk material and thus eliminates the box geometry dependency and the difficulties with spot welds, which might become highly probable crack initiation sites. The same author also identified the EWF as the most suitable parameter for crack-related problems such as crash behaviour [75]. However, the final testing of component designs is still necessary, and here, the CIDR evaluation is useful.

7. Conclusions

This study investigated the crashworthiness of a third-generation TRIP-aided bainitic steel grade and a boron steel grade using both experimental methods and FE analysis. All steps from material characterisation, implementing the material and damage model into a commercial FE code, as well as validating the results using dynamic axial compression experiments and high-speed 3D-DIC were performed. After analysing the results, the following conclusions were made:

- The strain-rate dependency of the studied steel grades was low for the strain rates investigated, both regarding flow stress behaviour as well as final fracture strains at various triaxialities.
- High-speed imaging and 3D-DIC can effectively be used to evaluate the crashworthiness of components by allowing a detailed tracking of crack initiation, crack propagation, and the evolution of damage. The evaluated strain measurement is useful for the validation of simulation models.
- The proposed methodology based on high-speed imaging gives a good first approximation of the CIDR when only considering the CI at two points (critical intrusion and maximum intrusion). High-speed imaging reduces the number of crash box needed and enables the evaluation of the CI at the intermediate crush intrusions, and the complete set of CI:s improves the accuracy and reliability of the CIDR. The proposed methodology results in the CIDR agreeing well with previously published data by other authors.
- The crash index rating is subjective and geometry-dependent, making results difficult to compare beyond the specific setup. However, it is still an important property when validating final designs.

Author Contributions: Conceptualization, S.J. and J.K.; methodology, S.J. and J.K.; software, S.J. and J.K.; validation, S.J.; formal analysis, S.J.; investigation, S.J. and J.K.; resources, J.K.; data curation, S.J.; writing—original draft preparation, S.J.; writing—review and editing, J.K.; visualization, S.J.; supervision, J.K.; project administration, S.J. and J.K.; funding acquisition, J.K.; All authors have read and agreed to the published version of the manuscript.

Funding: This research was funded by the EU Horizon2020 project FormPlanet, grant number 814519, which is gratefully acknowledged.

Data Availability Statement: The data presented in this study are available on request from the corresponding author.

Acknowledgments: The authors would like to thank Jan Granström for his expertise in high-speed testing in the lab as well as ArcelorMittal for supplying the material. Thanks also to Stefan Marth for his expertise regarding stepwise modelling, as well as Erik Lundholm, Olle Sandin, and Jakob Lundin for contributing valuable input to the simulation setup. The authors (and not the acknowledged individuals) are solely responsible for possible errors, limitations, or shortcomings of this work.

Conflicts of Interest: The authors declare no conflict of interest.

Appendix A

Table A1. Two-dimensional DIC settings used for the TBF 1180 characterisation experiments for the input data to the SMM algorithm.

Hardware Parameters				
	Shear ($\eta \approx 0$)	Hole ($\eta \approx 0.33$)	R15 ($\eta \approx 0.45$)	R3.75 ($\eta \approx 0.58$)
Camera	Vision Research Phantom v1610/v2512, 1 Megapixel sensor			
Lens	Tokina AT-X Pro D Macro 100 mm			
Image scale (mm· px^{-1})	0.014	0.024	0.012	0.012
Image resolution (px· px)	640 × 480			
Image acquisition rate, 1/10/100 s^{-1} (Hz)	200/2000/20,000	200/2000/20,000	200/2000/20,000	(200–1000)/(1000–2000)/20,000
Patterning technique	Spray paint			
Analysis parameters				
Software	GOM ARAMIS 6.x			
Subset size (px (mm))	16 (0.22)	16 (0.38)	16 (0.19)	16 (0.19)
Step size (px (mm))	8 (0.11)	4 (0.19)	8 (0.10)	8 (0.10)
Subset shape	Rectangular			
Overlap (%)	50 × 50	75 × 75	50 × 50	50 × 50

Table A2. Two-dimensional DIC settings used for the PHS 1000 characterisation experiments for the input data to the SMM algorithm.

Hardware Parameters				
	Shear ($\eta \approx 0$)	Hole ($\eta \approx 0.33$)	R15 ($\eta \approx 0.45$)	R3.75 ($\eta \approx 0.58$)
Camera	Vision Research Phantom, 1 Megapixel sensor			
Lens	Tokina AT-X Pro D Macro 100 mm			
Image resolution (px· px)	640 × 480			
Image scale (mm· px^{-1})	0.014	0.024	0.012	0.012

Table A2. *Cont.*

Hardware Parameters				
Image acquisition rate, 1/10/100 s^{-1} (Hz)	400/4000/41,667	400/4000/41,667	400/4000/20,000	400/4000/20,000
Patterning technique	Spray paint			
Analysis parameters				
Software	GOM ARAMIS 6.x			
Subset size (px (mm))	16 (0.23)	16 (0.38)	16 (0.20)	16 (0.20)
Step size (px (mm))	8 (0.12)	4 (0.10)	8 (0.10)	8 (0.10)
Subset shape	Rectangular			
Overlap (%)	50 × 50	75 × 75	50 × 50	50 × 50

Table A3. Three-dimensional DIC settings used for the validation experiments for the crash boxes.

Hardware Parameters	
Cameras	Vision Research Phantom v1610/v2512 1 Megapixel sensor
Lenses	Sigma DG Macro f/2.8 50 mm
Angle (degrees)	22.8
Image resolution (px· px)	800 × 600
Image acquisition rate (Hz)	24,000
Patterning technique	Spray paint
Calibration results	
Calibration deviation (px)	0.033
Measuring volume (w/h/d) (mm)	240.1/255.5/255.5
Analysis parameters	
Software	GOM ARAMIS 6.x
Subset size (px (mm))	15
Step size (px (mm))	5
Subset shape	Rectangular
Overlap (%)	50

By performing an autocorrelation of a typical speckle pattern, the average speckle diameter can be estimated to the half of the diameter [76]. An example of a peak from a pattern belonging to one of the tensile specimens is shown in Figure A1a. The corresponding contour plot is depicted in the middle (b) showing a peak with a radius of approx. 2 × 4 pixels. A similar contour plot from one of the crash boxes with a radius of approx. 2 × 3.5 pixels is shown to right (c). Hence, the speckle size in all conducted experiments were between three and four pixels.

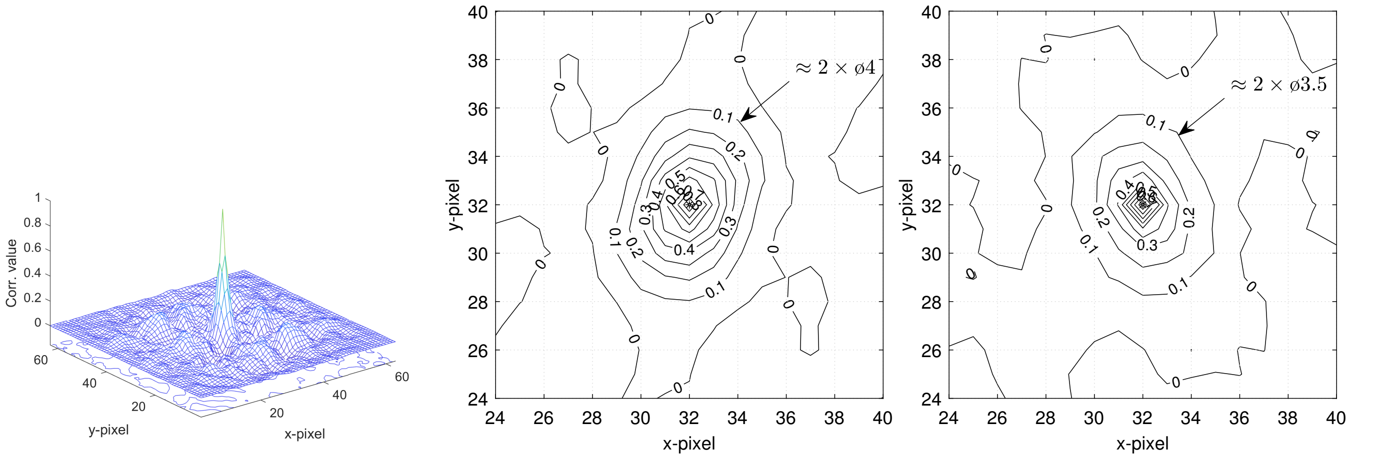

(**a**) Correlation peak (**b**) Contour plot—tensile specimen (**c**) Contour plot—crash box

Figure A1. Typical correlation peak obtained from the speckle patterns of one of the tensile specimens (**a**). Contour plot of a typical peak for a tensile specimen (**b**). Contour plot of a typical peak for a crash box (**c**).

References

1. Sullivan, J.L.; Hu, J. Life cycle energy analysis for automobiles. In *SAE Technical Papers*; SAE: Warrendale, PA, USA, 1995. [CrossRef]
2. MacLean, H.L.; Lave, L.B. Life Cycle Assessment of Automobile/Fuel Options. *Environ. Sci. Technol.* **2003**, *37*, 5445–5452. [CrossRef] [PubMed]
3. McAuley, J.W. Global Sustainability and Key Needs in Future Automotive Design. *Environ. Sci. Technol.* **2003**, *37*, 5414–5416. [CrossRef] [PubMed]
4. Keoleian, G.A.; Sullivan, J.L. Materials challenges and opportunities for enhancing the sustainability of automobiles. *MRS Bull.* **2012**, *37*, 365–372. [CrossRef]
5. Das, S.; Graziano, D.; Upadhyayula, V.K.; Masanet, E.; Riddle, M.; Cresko, J. Vehicle lightweighting energy use impacts in U.S. light-duty vehicle fleet. *Sustain. Mater. Technol.* **2016**, *8*, 5–13. [CrossRef]
6. Koffler, C.; Rohde-Brandenburger, K. On the calculation of fuel savings through lightweight design in automotive life cycle assessments. *Int. J. Life Cycle Assess.* **2010**, *15*, 128–135. [CrossRef]
7. Kim, H.C.; Wallington, T.J. Life cycle assessment of vehicle lightweighting: A physics-based model of mass-induced fuel consumption. *Environ. Sci. Technol.* **2013**, *47*, 14358–14366. [CrossRef]
8. Kim, H.C.; Wallington, T.J. Life Cycle Assessment of Vehicle Lightweighting: A Physics-Based Model to Estimate Use-Phase Fuel Consumption of Electrified Vehicles. *Environ. Sci. Technol.* **2016**, *50*, 11226–11233. [CrossRef]
9. Cecchel, S. Materials and technologies for lightweighting of structural parts for automotive applications: A review. *SAE Int. J. Mater. Manuf.* **2021**, *14*, 81–97. [CrossRef]
10. Witik, R.A.; Payet, J.; Michaud, V.; Ludwig, C.; Månson, J.A.E. Assessing the life cycle costs and environmental performance of lightweight materials in automobile applications. *Compos. Part A Appl. Sci. Manuf.* **2011**, *42*, 1694–1709. [CrossRef]
11. Zhang, W.; Xu, J. Advanced lightweight materials for Automobiles: A review. *Mater. Des.* **2022**, *221*, 110994. [CrossRef]
12. Kawajiri, K.; Kobayashi, M.; Sakamoto, K. Lightweight materials equal lightweight greenhouse gas emissions?: A historical analysis of greenhouse gases of vehicle material substitution. *J. Clean. Prod.* **2020**, *253*, 119805. [CrossRef]
13. Frómeta, D.; Tedesco, M.; Calvo, J.; Lara, A.; Molas, S.; Casellas, D. Assessing edge cracking resistance in AHSS automotive parts by the Essential Work of Fracture methodology. *J. Phys. Conf. Ser.* **2017**, *896*, 012102. [CrossRef]
14. Casellas, D.; Lara, A.; Frómeta, D.; Gutiérrez, D.; Molas, S.; Pérez, L.; Rehrl, J.; Suppan, C. Fracture Toughness to Understand Stretch-Flangeability and Edge Cracking Resistance in AHSS. *Metall. Mater. Trans. A Phys. Metall. Mater. Sci.* **2017**, *48*, 86–94. [CrossRef]
15. Karbasian, H.; Tekkaya, A. A review on hot stamping. *J. Mater. Process. Technol.* **2010**, *210*, 2103–2118. [CrossRef]
16. Noder, J.; Gutierrez, J.E.; Zhumagulov, A.; Dykeman, J.; Ezzat, H.; Butcher, C. A comparative evaluation of third-generation advanced high-strength steels for automotive forming and crash applications. *Materials* **2021**, *14*, 4970. [CrossRef]
17. Frómeta, D.; Lara, A.; Grifé, L.; Dieudonné, T.; Dietsch, P.; Rehrl, J.; Suppan, C.; Casellas, D.; Calvo, J. Fracture Resistance of Advanced High-Strength Steel Sheets for Automotive Applications. *Metall. Mater. Trans. A Phys. Metall. Mater. Sci.* **2021**, *52*, 840–856. [CrossRef]
18. Savic, V.; Hector, L.; Alturk, R.; Enloe, C. High Strain Rate Tensile Behavior of 1180MPa Grade Advanced High Strength Steels. In *SAE Technical Papers*; SAE: Warrendale, PA, USA, 2020. [CrossRef]
19. Golling, S.; Frómeta, D.; Casellas, D.; Jonsén, P. Investigation on the influence of loading-rate on fracture toughness of AHSS grades. *Mater. Sci. Eng. A* **2018**, *726*, 332–341. [CrossRef]

20. Marth, S.; Häggblad, H.Å.; Oldenburg, M.; Östlund, R. Post necking characterisation for sheet metal materials using full field measurement. *J. Mater. Process. Technol.* **2016**, *238*, 315–324. [CrossRef]
21. Marth, S.; Häggblad, H.Å.; Oldenburg, M. A comparison between stepwise modelling and inverse modelling methods for characterization of press hardened sheet metals. In Proceedings of the 6th International Conference Hot Sheet Metal Forming of High-Performance Steel CHS2, Atlanta, GA, USA, 4–7 June 2017; pp. 281–288.
22. Sjöberg, T.; Marth, S.; Kajberg, J.; Häggblad, H.Å. Experimental characterisation of the evolution of triaxiality stress state for sheet metal materials. *Eur. J. Mech. A/Solids* **2017**, *66*, 279–286. [CrossRef]
23. Marth, S.; Djebien, S.; Kajberg, J.; Häggblad, H.Å. Stepwise modelling method for post necking characterisation of anisotropic sheet metal. *Model. Simul. Mater. Sci. Eng.* **2021**, *29*, 085001. [CrossRef]
24. Sjöberg, T.; Kajberg, J.; Oldenburg, M. Calibration and validation of three fracture criteria for alloy 718 subjected to high strain rates and elevated temperatures. *Eur. J. Mech. A/Solids* **2018**, *71*, 34–50. [CrossRef]
25. Larour, P.; Pauli, H.; Kurz, T.; Hebesberger, T. Influence of post uniform tensile and bending properties on the crash behaviour of AHSS and press-hardening steel grades. In Proceedings of the 2010 IDDRG Conference, Graz, Austria, 31 May–2 June 2010; pp. 107–126.
26. Walp, M.S. Impact dependent properties of advanced and ultra high strength steels. In *SAE Technical Papers*; SAE: Warrendale, PA, USA, 2007. [CrossRef]
27. Larour, P.; Naito, J.; Pichler, A.; Kurz, T.; Murakami, T. Side impact crash behavior of press-hardened steels—Correlation with mechanical properties. In Proceedings of the 5th International Conference on Hot Sheet Metal Forming of High-Performance Steel, Toronto, ON, Canada, 31 May–3 June 2015; pp. 281–289.
28. Frómeta, D.; Lara, A.; Molas, S.; Casellas, D.; Rehrl, J.; Suppan, C.; Larour, P.; Calvo, J. On the correlation between fracture toughness and crash resistance of advanced high strength steels. *Eng. Fract. Mech.* **2019**, *205*, 319–332. [CrossRef]
29. Barnwal, V.K.; Lee, S.Y.; Choi, J.; Kim, J.H.; Barlat, F. Fracture assessment in dual phase and transformation-induced plasticity steels during 3-point bending. *Theor. Appl. Fract. Mech.* **2020**, *110*, 102834. [CrossRef]
30. Gutierrez, J.E.; Noder, J.; Butcher, C. Experimental characterization and deterministic prediction of in-plane formability of 3rd generation advanced high strength steels. *Metals* **2020**, *10*, 902. [CrossRef]
31. Noder, J.; Gutierrez, J.E.; Zhumagulov, A.; Khameneh, F.; Ezzat, H.; Dykeman, J.; Butcher, C. Constitutive, Formability, and Fracture Characterization of 3rd Gen AHSS with an Ultimate Tensile Strength of 1180 MPa. *SAE Int. J. Adv. Curr. Pract. Mobil.* **2021**, *3*, 1395–1407. [CrossRef]
32. Abedini, A.; Noder, J.; Kohar, C.P.; Butcher, C.J. Accounting for Shear Anisotropy and Material Frame Rotation on the Constitutive Characterization of Automotive Alloys using Simple Shear Tests. *Mech. Mater.* **2020**, *148*, 103419. [CrossRef]
33. Sandin, O.; Jonsén, P.; Frómeta, D.; Casellas, D. Stating failure modelling limitations of high strength sheets: Implications to sheet metal forming. *Materials* **2021**, *14*, 821. [CrossRef]
34. International Digital Image Correlation Society; Jones, E.; Iadicola, M.E. *A Good Practices Guide for Digital Image Correlation*; International Digital Image Correlation Society: Boston, MA, USA, 2018. [CrossRef]
35. Johnson, G.R.; Cook, W.H. A constitutive model and data for metals subjected to large strains, high strain rates, and high temperatures. In Proceedings of the 7th International Symposium on Ballistics, The Hague, The Netherlands, 19–21 April 1983; pp. 541–547.
36. Rice, J.; Tracey, D. On the ductile enlargement of voids in triaxial stress fields. *J. Mech. Phys. Solids* **1969**, *17*, 201–217. [CrossRef]
37. McClintock, F.A. A Criterion for Ductile Fracture by the Growth of Holes. *J. Appl. Mech.* **1968**, *35*, 363–371. [CrossRef]
38. Mackenzie, A.; Hancock, J.; Brown, D. On the influence of state of stress on ductile failure initiation in high strength steels. *Eng. Fract. Mech.* **1977**, *9*, 167–188. [CrossRef]
39. Sun, J. Effect of stress triaxiality on micro-mechanisms of void coalesence and micro-fracture ductility of materials. *Eng. Fract. Mech.* **1991**, *39*, 799–805. [CrossRef]
40. Bao, Y.; Wierzbicki, T. On fracture locus in the equivalent strain and stress triaxiality space. *Int. J. Mech. Sci.* **2004**, *46*, 81–98. [CrossRef]
41. Bao, Y.; Wierzbicki, T. On the cut-off value of negative triaxiality for fracture. *Eng. Fract. Mech.* **2005**, *72*, 1049–1069. [CrossRef]
42. Johnson, G.R.; Cook, W.H. Fracture characteristics of three metals subjected to various strains, strain rates, temperatures and pressures. *Eng. Fract. Mech.* **1985**, *21*, 31–48. [CrossRef]
43. Wierzbicki, T.; Bao, Y.; Lee, Y.W.; Bai, Y. Calibration and evaluation of seven fracture models. *Int. J. Mech. Sci.* **2005**, *47*, 719–743. [CrossRef]
44. Teng, X.; Wierzbicki, T. Evaluation of six fracture models in high velocity perforation. *Eng. Fract. Mech.* **2006**, *73*, 1653–1678. [CrossRef]
45. Bai, Y.; Wierzbicki, T. Application of extended Mohr-Coulomb criterion to ductile fracture. *Int. J. Fract.* **2010**, *161*, 1–20. [CrossRef]
46. Bai, Y.; Wierzbicki, T. A new model of metal plasticity and fracture with pressure and Lode dependence. *Int. J. Plast.* **2008**, *24*, 1071–1096. [CrossRef]
47. Benzerga, A.; Surovik, D.; Keralavarma, S. On the path-dependence of the fracture locus in ductile materials—Analysis. *Int. J. Plast.* **2012**, *37*, 157–170. [CrossRef]
48. Basu, S.; Benzerga, A.A. On the path-dependence of the fracture locus in ductile materials: Experiments. *Int. J. Solids Struct.* **2015**, *71*, 79–90. [CrossRef]

49. Huang, G.; Tihay, K.; Sriram, S.; Weber, B.; Dietsch, P.; Cornette, D. Fracture characterization of AHSS using two different experimental methods. *Iop Conf. Ser. Mater. Sci. Eng.* **2018**, *418*, 012080. [CrossRef]
50. Reu, P. All about speckles: Aliasing. *Exp. Tech.* **2014**, *38*, 1–3. [CrossRef]
51. Reu, P. All about speckles: Speckle size measurement. *Exp. Tech.* **2014**, *38*, 1–2. [CrossRef]
52. Neukamm, F.; Feucht, M.; Haufe, A.D. Consistent Damage Modelling in the Process Chain of Forming to Crashworthiness Simulations. In Proceedings of the LS-Dyna Anwenderforum, Bamberg, Germany, 30 September–1 October 2008.
53. Neukamm, F.; Feucht, M.; Roll, K.; Haufe, A. On closing the Constitutive Gap between Forming and Crash Simulation. In Proceedings of the 10th International LS-DYNA Users Conference, Detroit, MI, USA, 8–10 June 2008.
54. Neukamm, F.; Feucht, M.; Haufe, A. Considering damage history in crashworthiness Simulations. In Proceedings of the 7th European LS-Dyna Conference, Salzburg, Austria, 14–15 May 2009.
55. Andrade, F.; Feucht, M.; Haufe, A.D. On the Prediction of Material Failure in LS-DYNA®: A Comparison Between GISSMO and DIEM. In Proceedings of the 13th European LS-DYNA Users Conference 2014, Dearborn, MI, USA, 8–10 June 2014.
56. Chen, G.; Huang, L.; Link, T.M.; Tyan, T.; Aekbote, K. *Calibration and Validation of GISSMO Damage Model for A 780-MPa Third Generation Advanced High Strength Steel*; SAE: Warrendale, PA, USA, 2020. [CrossRef]
57. Chen, X.; Chen, G.; Huang, L. Validation of GISSMO Model for Fracture Prediction of a Third-Generation Advanced High-Strength Steel. *SAE Int. J. Mater. Manf.* **2018**, *11*, 293–302. [CrossRef]
58. Caro, L.P.; Schill, M.; Haller, K.; Odenberger, E.L.; Oldenburg, M. Damage and fracture during sheet-metal forming of alloy 718. *Int. J. Mater. Form.* **2020**, *13*, 15–28. [CrossRef]
59. Samadian, P.; ten Kortenaar, L.; Omer, K.; Butcher, C.; Worswick, M.J. Fracture characterization of tailored Usibor® 1500-AS and damage modelling based on a coupled-micromechanical-phenomenological strategy. *Eng. Fract. Mech.* **2020**, *223*, 106785. [CrossRef]
60. Considére, M. *L'Emploi du Fer de l'Acier Dans les Constructions, Memoire No 34*; Annales des Ponts et Chaussées: Paris, France, 1885; pp. 574–575.
61. Swift, H. Plastic instability under plane stress. *J. Mech. Phys. Solids* **1952**, *1*, 1–18. [CrossRef]
62. Marciniak, Z.; Kuczyński, K. Limit strains in the processes of stretch-forming sheet metal. *Int. J. Mech. Sci.* **1967**, *9*, 609–612, IN1–IN2, 613–620. [CrossRef]
63. Hill, R. On discontinuous plastic states, with special reference to localized necking in thin sheets. *J. Mech. Phys. Solids* **1952**, *1*, 19–30. [CrossRef]
64. Stören, S.; Rice, J.R. Localized necking in thin sheets. *J. Mech. Phys. Solids* **1975**, *23*, 421–441. [CrossRef]
65. Hora, P.; Tong, L.; Berisha, B. Modified maximum force criterion, a model for the theoretical prediction of forming limit curves. *Int. J. Mater. Form.* **2013**, *6*, 267–279. [CrossRef]
66. Abedini, A.; Butcher, C.J.; Worswick, M.J. Fracture characterization of ZEK100 magnesium alloy sheet under monotonic and non-proportional loading histories. *IOP Conf. Ser. Mater. Sci. Eng.* **2018**, *418*, 012075. [CrossRef]
67. De Borst, R.; Sluys, L.; Mühlhaus, H.B.; Pamin, J. Fundamental issues in finite element analyses of localization of deformation. *Eng. Comput.* **1993**, *10*, 99–121. [CrossRef]
68. Andrade, F.X.C.; Feucht, M.; Haufe, A.; Neukamm, F. An incremental stress state dependent damage model for ductile failure prediction. *Int. J. Fract.* **2016**, *200*, 127–150. [CrossRef]
69. Pack, K.; Mohr, D. Combined necking & fracture model to predict ductile failure with shell finite elements. *Eng. Fract. Mech.* **2017**, *182*, 32–51. [CrossRef]
70. Jun, H.; Grant, T.; Campbell, C. True Fracture Strain Measurement and Derivation for Advanced High-Strength Steel Sheets. *SAE Int. J. Adv. Curr. Pract. Mobil.* **2022**, *4*, 1394–1402. [CrossRef]
71. *ISO 6487:2015*; Road Vehicles—Measurement Techniques in Impact Tests—Instrumentation. International Organization for Standardization: Geneva, Switzerland, 2015.
72. Jayakumar, S.; Hajdarevic, A.; Anand, S.; Fang, X. Experimental and FE analyses of the crushing and bending behaviors of GMT and hybrid-formed Al-GMT structures. *Thin-Walled Struct.* **2023**, *186*, 110648. [CrossRef]
73. Cotterell, B.; Reddel, J. The essential work of plane stress ductile fracture. *Int. J. Fract.* **1977**, *13*, 267–277. [CrossRef]
74. Clutton, E. Essential work of fracture. In *Fracture Mechanics Testing Methods for Polymers, Adhesives and Composites*; Moore, D., Pavan, A., Williams, J., Eds.; Elsevier: Amsterdam, The Netherlands; European Structural Integrity Society: Cassino, Italy, 2001; Volume 28, pp. 177–195. [CrossRef]
75. Frómeta, D.; Parareda, S.; Lara, A.; Molas, S.; Casellas, D.; Jonsén, P.; Calvo, J. Identification of fracture toughness parameters to understand the fracture resistance of advanced high strength sheet steels. *Eng. Fract. Mech.* **2020**, *229*, 106949. [CrossRef]
76. Sjödahl, M. Accuracy in electronic speckle photography. *Appl. Opt.* **1997**, *36*, 2875–2885. [CrossRef]